



저작자표시-비영리-변경금지 2.0 대한민국

이용자는 아래의 조건을 따르는 경우에 한하여 자유롭게

- 이 저작물을 복제, 배포, 전송, 전시, 공연 및 방송할 수 있습니다.

다음과 같은 조건을 따라야 합니다:



저작자표시. 귀하는 원저작자를 표시하여야 합니다.



비영리. 귀하는 이 저작물을 영리 목적으로 이용할 수 없습니다.



변경금지. 귀하는 이 저작물을 개작, 변형 또는 가공할 수 없습니다.

- 귀하는, 이 저작물의 재이용이나 배포의 경우, 이 저작물에 적용된 이용허락조건을 명확하게 나타내어야 합니다.
- 저작권자로부터 별도의 허가를 받으면 이러한 조건들은 적용되지 않습니다.

저작권법에 따른 이용자의 권리는 위의 내용에 의하여 영향을 받지 않습니다.

이것은 [이용허락규약\(Legal Code\)](#)을 이해하기 쉽게 요약한 것입니다.

[Disclaimer](#)

공학박사 학위논문

Surface Functionalization of Metallic Bio-implant

금속 생체 임플란트의 표면 기능화

2021년 8월

서울대학교 대학원

재료공학부

이 민 규

Surface Functionalization of Metallic Bio-implant

금속 생체 임플란트의 표면 기능화

지도 교수 김 현 이

이 논문을 공학박사 학위논문으로 제출함

2021년 8월

서울대학교 대학원

재료공학부

이 민 규

이 민 규의 박사 학위논문을 인준함

2021년 8월

위 원 장 선 정 윤

부위원장 김 현 이

위 원 강 승 균

위 원 장 태 식

위 원 정 현 도

Abstract

Surface Functionalization of Metallic Bio-implant

Minkyu Lee

Department of Materials Science and Engineering

Seoul National University

Metals have been widely used in biomedical fields for decades due to its excellent biocompatibility and strength. Metallic medical implants such as vascular stents, bone and dental implants can support and replace impaired tissue successfully. However, irregular corrosion behavior and severe inflammatory reactions in the body after implantation are the biggest problems limiting its application. Therefore, to solve these problems, a surface treatment method for imparting various bio-functionality to the surface of metallic bio-implant is widely utilized. The metal and drug coating methods on the surface are the simplest and most convenient way to enhance bio-functionality of metallic implants. In spite of these achievements, it showed the delamination of the coating layers due to poor coating stability leading to the adverse effects in host tissue.

In this study, we developed a simple and effective surface treatment method for metallic bio-implants using a DC magnetron sputtering. The Target-ion induced plasma sputtering (TIPS) is a metal etching technique using accelerated metal cations emitted from the target. The metal cations emitted from the target are accelerated by an extremely high negative voltage applied to the metal substrates which inflict a high impact energy on substrate substance. TIPS treated metal substrates show unique nanostructures injected with target metal ions/atoms, and these surfaces have a variety of bio-functions. The target metal ions, accelerated by the high negative substrate voltage and strongly injected into the substrate, have excellent mechanical stability between target materials and metal substrates compared to the existing convectional DC sputtering process. In particular, TIPS process etches the surface of metallic bio-implants with forming distinctive nanostructures which can offer various bio-functions such as controllable corrosion behavior and antibacterial activity. A tantalum (Ta) was introduced as a target material known as a biocompatible metal element. Besides, it has a high atomic weight which enables Ta to etch metallic substrate effectively.

In the first study, we invented Ta incorporated bare iron (Fe) platform for medical applications. In recent years, pure Fe has attracted significant attention as a promising biodegradable orthopedic implant material due to its excellent mechanical and biological properties. However, in physiological

conditions, Fe has an extremely slow degradation rate with localized degradation, which is problematic for practical applications. In this study, we developed a novel combination of a nanostructured surface topography and galvanic reaction to achieve uniform and accelerated degradation of an Fe implant. The TIPS technique was applied on the Fe implant to introduce biologically compatible and electrochemically noble tantalum (Ta) onto its surface and develop surface nano-galvanic couples. During the TIPS process, numerous Ta ions generated from the sputtering gun were directly implanted into the surface of the Fe implant by applying an extremely high negative substrate bias voltage, which enabled the generation of distinct nanostructures on the surface of the Fe implant with the incorporation of a considerable amount of Ta (~50 at%) on top of the nanostructured surface. Electrochemical tests revealed that the uniformly distributed nano-galvanic corrosion cells of the TIPS-treated sample (nano Ta-Fe) led to relatively uniform and accelerated surface degradation compared to that of bare Fe. Furthermore, the mechanical properties of nano Ta-Fe remained almost constant during a long-term *in vitro* immersion test (~ 40 weeks). Biocompatibility was also assessed on surfaces of bare Fe and nano Ta-Fe using *in vitro* osteoblast responses through direct and indirect contact assays and an *in vivo* rabbit femur medullary cavity implantation model. The results revealed that nano Ta-Fe not only enhanced cell adhesion and spreading on its surface, but also exhibited no signs of cellular or tissue toxicity. These results demonstrate the immense potential of Ta-

implanted surface nanostructures as an effective solution for the practical application of Fe-based orthopedic implants, ensuring long-term biosafety and clinical efficacy.

In the second study, we imitated the nano-topography of dragonfly wings via TIPS on Co-Cr implants for antibacterial activity. Bio-metals are promising materials in biomedical field due to their excellent mechanical properties. To reconstruct or replace damaged tissue in the body, metallic materials are widely used in the following forms: vascular stents, dental and bone implants. It has the advantage of supporting the impaired tissue successfully where loads are applied because of its excellent mechanical properties. Despite these advantages, the poor antibacterial activity of metallic implants induces serious inflammatory responses such as peri-implantitis and osteomyelitis, which limits its applications to medical implants. Therefore, previous research has been actively conducted to coat or load antibiotic agents such as silver and antibiotics to impart excellent antibacterial property to the surface of metallic implants. Although incorporated silver or antibiotics exhibit excellent antibacterial effects and alleviate the inflammation, but their use is limited due to the side effects causing toxicity to cells. Recently, *Elena P. Ivanova* et al. reported that nanostructures of the dragonfly wings physically rupture bacterial cell walls called by mechano-bactericidal effect. In this study, the nano-scale structure of the dragonfly wings, which has mechano-

bactericidal effect, is imitated by using TIPS technique, which is a novel strategy to modify the surface of metallic implants. After applying TIPS technique to Co-Cr implants, it not only showed excellent antibacterial effects against gram-negative and gram-positive bacteria, but also presented enhanced biocompatibility resulting from nano-topography which induces a strong cell adhesion. The approach for this research described here enable metallic implants to achieve both excellent antibacterial effect and enhanced biocompatibility simultaneously.

Keywords: Metallic bio-implants, Tantalum, Biodegradable materials, Biomimetics

Student number: 2016-20810

Contents

Abstract.....	i
List of Tables.....	ix
List of Figures.....	x
Chapter 1. Introduction	1
1.1. Metallic bio-implants and its limitation	2
1.2. Surface functionalization of metallic bio-implants.....	3
1.2.1. Plasma treatment	3
1.2.2. Antibacterial treatment	4
1.3. Target-ion Induced Plasma Sputtering.....	5
Chapter 2. Uniform and accelerated biodegradation of iron-based implants	7
2.1. Introduction.....	8
2.2. Materials and methods.....	13
2.3. Results and discussion.....	20
2.4. Conclusion.....	41
Chapter 3. Bio-inspired Cobalt-Chrome surface with both enhanced biological activity and bactericidal effect	53
3.1. Introduction.....	54
3.2. Materials and methods.....	57
3.3. Results and discussion.....	64

3.4. Conclusion.....	77
Chapter 4. Conclusion.....	88
4. Conclusion	89
References.....	90
Abstract (Korean).....	100

List of Tables

Table 1.1. Electrochemical degradation properties of bare Fe and nano Ta–Fe samples.

Table 1.2. Surface roughness parameters of bare Fe and nano Ta–Fe up to 40 weeks of immersion in simulated body fluid solutions.

Table 2.1. Average height, center to center distance, diameter and aspect ratio of nanospike for the comparison between dragonfly wing and Nano-spike Co-Cr.

List of Figures

Figure 1.1. Schematic diagram of a typical sputtering and Targer-ion Induced Plasma Sputtering system

Figure 2.1. Representative surface field-emission scanning electron microscopy (FE-SEM) images of (a), (b) bare Fe and (c), (d) nano Ta–Fe at low and high magnification. The inset in (d) displays the cross-sectional focused ion beam (FIB)/FE-SEM image of the surface of nano Ta–Fe. (e) Cross-sectional scanning transmission electron microscopy image of nano Ta–Fe with energy-dispersive X-ray spectroscopy mapping (inset), and (f) chemical compositions at three regions in e (p1: top, p2: middle, and p3: bottom).

Figure 2.2. Electrochemical corrosion behaviors: Scanning Kelvin Probe maps of (a) bare Fe, (b) nano Ta–Fe, (c) Potentiodynamic polarization curves, and (d) Nyquist plots.

Figure 2.3. *In vitro* degradation test for 28 days in simulated body fluid solution to observe the degradation pit formation and degradation rate. (A) Field-emission scanning electron microscopy (FE-SEM) images of surface morphology of bare Fe and nano Ta–Fe at (a), (c) low magnification and (b), (d) high magnification, and (f) cross-sectional focused ion beam (FIB)/FE-SEM image of nano Ta–Fe. (B) Thickness of degradation byproducts (abbreviations Min. and Max. denote the minimum and maximum thickness, respectively, of the degradation byproducts). (C) Degradation depth of bare Fe and nano Ta–Fe. (D) Released Fe ion concentration of bare Fe and nano Ta–Fe.

Figure 2.4. (A) Optical images of bare Fe and nano Ta–Fe before and after 12 and 40 weeks of immersion in simulated body fluid solution. The inset scale bar is 500 μm . (B) Tensile tests of bare Fe and nano Ta–Fe up to 40 weeks of

immersion; (a) thickness loss, (b) stress–strain curves, (c) ultimate tensile strength, and (d) elongation rate (*: $p < 0.05$ and **: $p < 0.005$). (C) Three-dimensional surface topography as a function of immersion period using a laser scanning microscope.

Figure 2.5. (A) Water contact angles of bare Fe and nano Ta–Fe. (B) Low-magnification confocal laser scanning microscopy and high-magnification field-emission scanning electron microscopy (FE-SEM) images of attached osteoblast cells (MC3T3) on bare Fe and nano Ta–Fe surfaces after culturing for 6, 24, and 72 h. (C) Osteoblast cell viability in extracted culturing media with bare Fe and nano Ta–Fe immersions. (D) Representative FE-SEM images of adhered platelets on the surface of bare Fe and nano Ta–Fe. (E) Adhered platelet density on the bare Fe and nano Ta–Fe surface. (*: $p < 0.05$ and **: $p < 0.005$)

Figure 2.6. (A) Three-dimensional (3D) reconstruction images of micro-computed tomography scans after 4 and 16 weeks of *in vivo* experiments. (B) Residual volume of bare Fe and nano Ta–Fe after 4 and 16 weeks. Statistical significance is indicated as * ($p < 0.05$). (C) Scanning electron microscopy images and corresponding energy-dispersive X-ray spectroscopy mapping images obtained from rectangular regions in the cross sections of bare Fe and nano Ta–Fe after 4 and 16 weeks of *in vivo* degradation testing (oxygen: light blue, iron: red, and carbon: green).

Figure 2.7. *In vivo* histological and immunohistochemical characterization of the rabbit femur bone marrow implantation study. (A) Hematoxylin–eosin (H&E), (B) Prussian blue, and (C) CD68+ stained mid-diaphyseal femoral cross sections. The average thickness of Fe ions released into the bone marrow tissue and the number of CD68+ macrophages in the bone marrow of the rabbit are presented in (B) and (C), respectively, as a function of *in vivo* implantation

time. Black stars in (B) indicate the implant inserted regions. Statistical significance is indicated as ** ($p < 0.005$).

Figure 2.8. Schematic diagram of the TIPS process for Fe implants with Ta sputter target and negative substrate bias voltage of 1,000 V.

Figure 2.9. Representative surface field-emission scanning electron microscopy images of Fe samples with different negative substrate bias voltages for TIPS surface treatment: (a) 0 V, (b) 250 V, (c) 500 V, (d) 750 V and (e) 1000 V.

Figure 3.1. Representative surface morphologies of Flat, Ta coated, Nano-spike, and Nano-ripple: (a) field-emission scanning electron microscopy (FE-SEM), (b) the cross-sectional focused ion beam (FIB)/FE-SEM, and (c) Three-dimensional (3D) atomic force microscopy images. (Scale bar = 500 nm)

Figure 3.2. Cross-sectional scanning transmission electron microscopy image of Nano-spike Co-Cr with energy-dispersive X-ray spectroscopy mapping (Co-Cr and Ta elements), and chemical compositions at three regions in TEM image (p1: top, p2: middle, and p3: bottom). (Scale bar = 500 nm)

Figure 3.3. Water contact angles of Flat, Ta coated, Nano-spike, and Nano-ripple Co-Cr. Inset images denotes optical images of water droplets on each surface. (vs. Flat Co-Cr: $*p < 0.05$)

Figure 3.4. (A) Fluorescent images and FE-SEM images of *E. coli* and *S. aureus* cultured on Flat, Ta coated, Nano-spike, and Nano-ripple Co-Cr surfaces. The green and red fluorescence represent live and dead bacteria, respectively. The scale bar in the fluorescent CLSM and FE-SEM images are 10 μm and 500 nm, respectively. (B) Optical images of bacterial colony formation on agar plate after 12 hr of *E. coli* and *S. aureus* incubation. (C) The percentage of dead

bacteria on Flat, Ta coated, Nano-spike, and Nano-ripple Co-Cr calculated by CLSM images. (D) Bacteria colony count of *E. coli* and *S. aureus* estimated using optical images of bacteria colony formation. White scale bars indicate 10 μm and 500 nm for fluorescent CLSM and FE-SEM images, respectively. (vs. Flat Co-Cr: $*p < 0.05$)

Figure 3.5. (A) Low (upper) and high (lower) magnification CLSM images of osteoblast cells adhered on the surfaces of Flat, Ta coated, Nano-spike, and Nano-ripple Co-Cr. (B) The surface coverage rate of osteoblast cells on Flat, Ta coated, Nano-spike, and Nano-ripple Co-Cr quantified from CLSM images. (C) Cell proliferation, and (D) differentiation (ALP activity) of osteoblast cells on each sample after 1, 3, and 6 days and 14 days, respectively. (vs. Flat Co-Cr: $*p < 0.05$, and vs. Ta coated Co-Cr: $\#p < 0.05$)

Figure 3.6. Low (upper) and high (lower) magnification CLSM images of osteoblast cells on the surfaces of Flat, Ta coated, Nano-spike, and Nano-ripple Co-Cr co-cultured with (A) *E. coli* and (B) *S. aureus*, respectively. The insets at the left corner of high magnification images are FE-SEM images of *E. coli* and *S. aureus* on each surface. (C) The surface coverage rate of live osteoblast cells after 24 hr of co-culturing with *E. coli* and *S. aureus*. (vs. Flat Co-Cr: $*p < 0.05$, and vs. Nano-ripple: $\#p < 0.05$)

Figure 3.7. Schematic diagram of multi-functional Co-Cr bio-implants via Target-ion Induced Plasma Sputtering.

Chapter 1.

Introduction

1.1. Metallic bio-implants and its limitation

With an increase in expected lifespan, various diseases related to hard and soft tissues have emerged as critical problems in biomedical fields. In particular, the number of patients suffering from dental, bone, and vascular related diseases has increased significantly. As aging progresses, the strength of teeth and bones generally decreases, which makes it vulnerable to physical impact. Blood vessels are tissues that are more closely associated with human aging. The elasticity of blood vessels is reduced, and the accumulation of impurities in the blood vessels causes serious diseases such as arteriosclerosis and myocardial infarction [1]. To solve these problems, research on biomaterials for vascular, dental, and orthopedic implants has been actively conducted [2, 3]. Bio-implant materials are substance that is artificially inserted to treat or replace damaged tissues in the body. Ti-based implant materials are targeted to replace damaged teeth [4], and Fe-based are used to support fractured or damaged bone [5]. Co-based materials are utilized as vascular stents [6]. Due to their excellent mechanical property, damaged tissue can be effectively supported and healed.

Despite these advantages, metallic bio-implant materials have limitations such as non-uniform corrosion and bacterial infections due to their low antibacterial activity. Firstly, an irregular corrosion of biodegradable metals such as Mg, Zn and Fe leads to premature fracture of medical bio-

implants [7-9]. When biodegradable metals are used as bio-implants in the body, they will be subject to physical loads from host tissue. For example, biodegradable metal stents exhibited irregular corrosion in blood circulating system. As a result, the physical loads by blood vessels induce stress concentration in the area where the local corrosion of the stent has occurred leading to unexpected fracture of medical implants [10, 11]. Secondly, bacterial infections due to the poor antibacterial properties of metal implants are one of the most serious problems. Bacterial infections easily occur between the bio-implant and the tissue after surgery, which causes serious problems such as peri-implantitis and osteomyelitis [12-15].

1.2. Surface functionalization of metallic bio-implants

1.2.1. Plasma treatment

Various studies have been conducted to treat the problems of metallic bio-implant materials as described above [16, 17]. Plasma treatment is one of the most widely used methods for modifying the surface of metal implants which can impart surface chemistry, roughness, hydrophilicity, bio-functions to the surface of metallic bio-implants [18, 19]. Plasma treatment was introduced to treat irregular corrosion behavior of degradable metals. *J. Cheng et al.*

reported that Platinum (Pt) patterned Fe platform presented accelerated and uniform corrosion behaviors due to the presence of Pt which triggers galvanic corrosion reaction with Fe. In spite of these achievements, the noble metal coating method is vulnerable to mechanical deformation because of its poor coating stability with Fe [20]. These poor bonding between the coating layer of noble metals and Fe matrix have limitations that cannot be applied to bio-implants exposed to mechanical deformation such as stent expansion.

1.2.2. Antibacterial treatment

Various studies have been conducted to impart antibacterial properties to the bio-implant surface in order to solve the problem of implant infection due to low antibacterial properties. Firstly, antibacterial treatments of the implant surface are to coat or load silver or antibiotics [21, 22]. Silver is a typical metallic element with excellent antibacterial properties. *S.W. Kim* et al. reported that the the surface of Ti dental implant showed enhanced antibacterial activity by coating silver onto Ti surface. Secondly, Antibiotics also exhibited excellent antibacterial properties. Despite these achievements, toxicity to mammalian cells arising from the use of silver and antibiotics has been confirmed. It was demonstrated that increasing the amount of silver and antibiotics causes severe toxicity to mammalian cells [23].

1.3. Target-ion Induced Plasma Sputtering (TIPS)

TIPS technology was applied to overcome several limitations of bio-implant materials as mentioned above. The TIPS technology is illustrated in **Fig. 1**, which is a process of accelerating the metal cations emitted from the target toward the substrate to induce substrate etching. The existing sputtering process is a method in which metal cations emitted from the target are simply vapor-deposited on the substrate. On the other hand, in the TIPS system, the cations coming out of the target are accelerated in the direction of the substrate by an extremely high negative voltage applied to the substrate, giving a large impact energy to the substrate. The metal target materials used in this study is tantalum (Ta). Ta not only exhibits excellent biocompatibility, but also has a high atomic weight leading high etching efficiency in TIPS process. As a result, TIPS creates distinctive nano-structures on the surface of metal, which exhibits excellent osteoblast, fibroblast, and vascular cell affinity [6, 24-26]. In this research, we introduced TIPS technology to solve the limitations of metallic bio-implant materials.

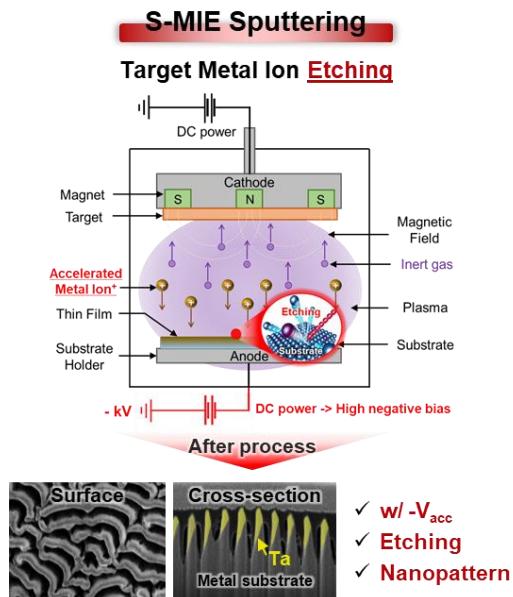
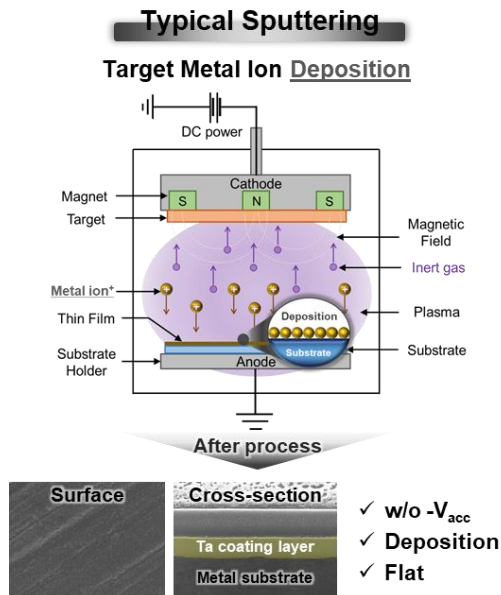


Figure 1.1. Schematic diagram of a typical sputtering and Target-ion Induced Plasma Sputtering (TIPS) system

Chapter 2.

Uniform and accelerated biodegradation of iron-based implants

2.1. Introduction

In past few decades, biodegradable metallic materials have undoubtedly served as one of the most promising strategies in regenerative medicine [27, 28]. Biodegradable metals possess excellent mechanical properties providing sufficient temporary support to resist the applied load, whereas the potential risk of long-term complications is essentially eliminated through their progressive degradation in the body. Therefore ideally, biodegradable metallic implants are best suited for the purposes of stabilization of fractured bone tissues and guidance of bone healing [3, 29]. However, from the biological safety aspect, there are strict requirements for material selection, including desirable degradation rates, balanced decline of mechanical properties with bone remodeling, and metabolism of the degradation byproducts in the body. To date, three types of metals have been recognized as a promising candidate for the development of biodegradable orthopedic implants: magnesium (Mg), zinc (Zn), and iron (Fe) [30-32]. Mg is primarily distributed in bone tissue and a key mineral in the development of bone mass and bone strength. Zn is widely acknowledged as a nutrient element for various biological process including enzyme function and immune competence [33]. However, unfortunately, most of Mg-based implants degrade too rapidly in physiological environments, losing their shape and strength before the injured tissues healed [34, 35], whereas Zn is not strong enough for load-bearing implantable devices [36].

Fe is the most abundant metal element in the human body and participates in a wide variety of metabolic processes, such as oxygen transport, energy metabolism, enzyme function, and DNA synthesis [37]. In particular, it is well known for its vital role in bone homeostasis, and its deficiency causes bone disorders and impairs bone mineralization. Previous studies have proven that Fe possesses better mechanical performance than most of metals and exhibits no local or systemic toxicity in both short- and long-term *in vivo* studies [38, 39]. However, despite its immense potential for the use as biodegradable orthopedic implants, the very low degradation rate of Fe in physiological media becomes a main obstacle for its successful clinical applications [40, 41]. Since long-lasting biodegradable materials in the body can act like permanent materials, Fe implants inevitably provoke chronic foreign body reactions, thereby causing implant loosening and eventual failure. In addition, the body fluids containing aggressive anions, such as chloride ions, can prompt localized preferential dissolutions of Fe and lead to the formation of sharp, deep, and narrow pits on its surface, which will significantly deteriorate the comprehensive mechanical performances and structural integrity of the Fe implant during its clinical service [42, 43].

Practically, it is relatively simple and feasible to enhance the degradation rate of Fe by adding additional metal elements, but it is more important to optimize the interface interaction between the implant and

surrounding bone tissues. Results of the past studies have shown that it remains difficult to obtain satisfactory combination of high biodegradation rate and reliable mechanical support without deteriorating biocompatibility. For instance, metallic Fe alloying has been shown to be very effective in enhancing degradation rate and mechanical properties by forming noble second phases into the Fe matrix, but cytotoxicity is also associated with the introduced metallic elements, such as manganese, cobalt, aluminum, tungsten, and palladium [5, 44, 45]. Since small quantities of these elements can severely deteriorate the cytocompatibility of Fe implants, more recent studies have been directed toward the surface modification of Fe without altering its bulk composition. Even in case of introducing additional materials, the surface modification approach can offer a large pool of biocompatible material candidates and a high degree of freedom in designing the structure and optimizing the degradation rate of the Fe implant. Zhou et al. developed micro-roughened Fe surface via sandblasting process which possessed high specific surface area ensuring physically accelerated degradation behavior of Fe under body fluid conditions [46]. *J. Cheng* et al. deposited micro-patterned gold disc films on the surface of Fe that generated micro-galvanic corrosion between Fe and gold under simulated body conditions and led to the significant increase of Fe degradation rate. *Huang* et al. revealed that the smaller platinum surface patterns (down to 4 μm) were more effective to accelerate degradation rate of Fe via formation of plenty of galvanic cells with the Fe matrix. However, these

micro-scale surface structures merely stimulated electrochemical reactions occurring on the Fe surface in physiological environment, while not inducing any favorable bone tissue responses toward the implant surface due to their inert biological nature.

Over several decades, it has been proven that nano-architected surfaces influence a wide range of physical and biological phenomena due to their extremely large surface areas and size similarity with extracellular matrix. Most of mammalian cells can specifically recognize nano-scaled topographical features and directly respond by conforming their adhesion morphologies to their surroundings and regulating their subsequent cellular behaviors such as survival, migration, proliferation, and differentiation [4, 47, 48]. However, despite these promising features, there has been no attempt to explore its capabilities to modulate both the degradation rate and cellular responses of the Fe implants. In this study, we develop a novel combination of nanostructured surface and noble metal ion implantation as physical and electrochemical cues for the purposes of high degradation rate and excellent bone tissue compatibility of the Fe implant. Recently developed target-ion induced plasma sputtering (TIPS) technique makes it possible to generate surface nano-patterns onto metallic substrates via its massive ion bombardment and implantation capabilities [49]. In this technique, numerous target metal ions generated from the sputtering target gun are accelerated towards the substrate under applying

extremely high negative substrate bias voltage, which provides continuous implantation of target ions on and non-uniform re-sputtering from the metal substrate. This unique feature enables generation of distinct nanostructures on the substrate surfaces and incorporation of target metals into them. In order to produce nano-galvanic cells over the surface of Fe implant, we introduce tantalum (Ta) as a sputtering target; Ta has a much higher corrosion potential (E_{corr}) than the pure Fe and is well-known for its favorable interactions with bone tissues [25, 50, 51]. After TIPS treatment, the surface morphology, microstructure, chemical composition, and electrochemical properties of the Fe implant (Nano Ta-Fe) were compared those of untreated Fe implant (Bare Fe). We then the rates of corrosion and cellular behaviors for the Fe implant before and after the TIPS treatment were compared using an *in vitro* and *in vivo* rabbit femoral defect model.

2.2. Materials and methods

Sample preparation

Commercial bare Fe (99.8%, Hosung Industry, Korea) with a square shape (10 mm × 10 mm × 2 mm) was purchased for the surface characterization, electrochemical test, *in vitro* degradation and cell viability test. All the samples were cleaned by ultrasonification in ethanol 10 min before the tantalum (Ta) incorporation process. A Ta target (75 mm diameter, 5 mm thickness, 99.99% purity, Avention, Korea) was located in a DC magnetron sputtering gun (Ultech Co. Ltd, Daegu, Korea). A vacuum chamber was sequentially pumped down to 5×10^{-4} Pa with rotary and diffusion pumps. To create enough amounts of Ta ions, 50 W of target power was directly applied to the Ta target, and the working temperature and pressure were retained at 0.6 Pa and 25 °C, respectively, during the process. A negative bias voltage (−1000 V) was supplied to the Fe substrate. The Ta implanted Fe were designated as nano Ta-Fe.

Surface characterization

Surface morphology was confirmed using field-emission scanning electron microscopy (FE-SEM; JSM-6330F, JEOL, Japan). The compositional analysis of nano Ta-Fe was carried out with high-resolution transmission

electron microscopy (TEM; JEM-2100F, JEOL, Japan) conducted at 200 kV. The Ta distribution profile on Fe surfaces was measured by energy-dispersive X-ray spectroscopy (EDS) elemental spot analysis mode in TEM. The cross-sectional image and EDS mapping of nano Ta-Fe surface after *in vitro* and *in vivo* degradation tests were observed by focused ion beam milling and FE-SEM equipped with an EDS (FIB/FE-SEM; AURIGA, Carl Zeiss, Germany).

Electrochemical test

Electrochemical measurements were conducted with three-electrode system using a potentiostat/galvanostat (Model 273, EG&G Princeton Applied Research, USA). A saturated calomel electrode (SCE) was utilized as a reference electrode and platinum coil were acted as a counter electrode. All the samples were completely immersed in 1 L of SBF solution adjusted to pH 7.4 at 37 ± 0.5 °C. with an exposed area of 1 cm². The open circuit potential (OCP) was measured for 1 hr. Electrochemical impedance spectroscopy (EIS) was recorded from 100 kHz to 10 mHz at OCP value. The potentiodynamic polarization curves were achieved ranging from OCP value ± 600 mV vs. SCE at a scanning rate of 1 mV·s⁻¹. In addition, the surface voltage potential of samples was measured by a scanning kelvin probe mode of AFM (NX-10, Park systems, Korea). The scanning area was 25 μm \times 25 μm . The tests were performed at 25 °C in air.

***In vitro* static degradation test**

In vitro static degradation tests were conducted at 37 °C in SBF solution for 1, 14, and 28 days. After immersion tests, all the samples were gently rinsed with ethanol and ultrasonically cleaned for an hour to prevent further degradation and observe the surface morphology of the corroded Fe substrates. The structural change of surface morphologies as a function of immersion period was investigated by FE-SEM furnished with an EDS attachment. The amount of Fe ion release in 25 ml SBF solution was recorded by conducting inductively coupled plasma mass spectrometry (ICP-MS; Varian 820-MS, Varian, Australia) after static immersion test.

***In vitro* degradation and mechanical property evaluation**

In vitro degradation test was performed to check the mechanical properties change as a function of degradation time. Mechanical stability after degradation was assessed over immersion time for 12 and 40 weeks. The dog-bone samples with the thickness of 450 µm was used for degradation and mechanical test in accordance with ASTM E 8/E 8M-08. All the samples were immersed SBF solution and temperature was maintained at 37 °C. To make accelerated environment for the degradation, SBF was replaced every 2 days for 40 weeks. After 12 and 40 weeks of immersion, all the samples were extracted from SBF solution and ultrasonically cleaned with ethanol to prevent

further degradation. The surface roughness of the samples was examined by laser scanning microscopy (LSM; OLS 4100, Olympus, Japan). A universal testing machine (Instron 5580, Instron Corp., USA) was used with a fixed loading rate of 1 mm/min. The change in the thickness of tested samples was measured to assess degradation behavior of bare and nano Ta-Fe.

***In vitro* cellular assays**

In vitro cytocompatibility of the bare and nano Ta-Fe was assessed with regard to cell attachment and proliferation with osteoblast cells (MC3T3-E1, CRL-2593, ATCC, USA). Incubated cells were seeded onto the bare Fe and nano Ta-Fe surfaces at the density of 2×10^4 cells/mL for the cell attachment and proliferation assays. The osteoblast cells were cultivated in a cell incubator containing 5 % CO₂ at 37 °C. A culturing medium (α -MEM, Welgene Co., Ltd., Korea) with 10 mM β -glycerophosphate (Sigma-Aldrich, USA), 10 μ g mL⁻¹ ascorbic acid, 1% penicillin-streptomycin and 10% fetal bovine serum (FBS) was used.

Cell attachment test of bare and nano Ta-Fe samples was conducted using fluoresce imaging for 1 and 3 days. All the samples were disinfected with absolute ethanol under ultraviolet (UV) irradiation overnight prior to cell seeding. The live cell staining was conducted by calcein acetoxymethyl ester (Calcein AM, Invitrogen, USA) for 40 min of incubation. After 1 and 3 days of

culturing, the morphologies of the attached cells were observed by confocal laser scanning microscopy (CLSM; C1 PLUS, Nikon, Japan).

Cell proliferation was assessed using MTS assay (MTS, Promega corp., USA) for 1 and 3 days. Extraction media of bare and nano Ta-Fe was used after 2 days of immersion in Dulbecco's modified Eagle's medium (DMEM, Gibco, Germany). Extraction medium (0.5 mL) was replaced to 24-well plate with 0.5 mL of DMEM. The control groups are DMEM containing 10% fetal bovine serum (FBS) or 10% dimethyl sulfoxide (DMSO) as a positive or negative control respectively [52]. Total cell seeding density of samples was 2×10^4 cells/mL. The amount of the formazan product was assessed after 1 and 3 days of culturing with the absorbance at 490 nm using microplate reader.

***In vitro* animal model and surgical procedure**

All the *in vivo* procedures containing animal selection, surgical protocol, management and sacrificial method were authorized by the Ethics Committee on Animal Experimentation of the Institutional Animal Care and Use Committee of GENOSS (GEN-IACUC, no. 1902-01). *In vivo* experiment was conducted using a bone marrow cavity model in male 12 weeks old New Zealand White rabbits (male, body weight 2.5-3.0 kg, DBL Inc., South Korea) as previously described [53, 54]. The rabbits were anesthetized by intramuscular injection method with an anesthetic mixture of xylazine (1.5 mL,

Rompun 2%, Bayer Korea, South Korea), tiletamine (0.5 mL, Zoletil, Virbac Lab, France), and a local anesthetic, lidocaine (0.5 mL with 1:100000 epinephrine, Yuhan Corporation, South Korea). A round hole (2 mm diameter) was created in the patellar groove using a hand drill. Bare and nano Ta-Fe pins (2 mm in diameter and 10 mm in height) were individually inserted in each bone marrow cavity in femur of each rabbit. The wounds were closed with sutures. A postoperative antibiotic, 0.3 mL of gentamicin (Samu Median, South Korea) in saline solution was carefully injected for 3 days. The rabbits were scarified after 1 and 4 months of implantation.

Micro-computed Topography (Micro-CT) analysis

In order to measure inserted pin position, femur bone tissues were visualized after sacrifice by micro-CT (Skyscan 1173, Skyscan, Belgium) under the specific condition (a voltage of 130 kV, a resolution of 6 μm , and a current of 60 μA). Post-processing software (NRecon and Data Viewer 1.4, Skyscan, USA) was used to reconstruct the three-dimensional (3D) and 2D images of the samples.

Histological evaluation

The samples for histological evaluation were divided into two parts.

One part was fixed in 10% formaldehyde solution and immersed in resin (Technovit 7200 VLC, Kulzer, Germany) for hematoxylin-eosin (H&E) staining. The other part of harvested bone was embedded in paraffin for Prussian blue and immunohistochemistry with primary anti-CD68 staining (CD68, abcam, USA). The slide of the blocks (thickness <5 μ m) were fabricated by cutting and grinding. The numbers of macrophages were calculated in the unit area of the image field. A panoramic digital slide scanner (Pannoramic 250 Flash III, 3DHISTECH Ltd., Hungary) was used to observe microscopic images of the stained sections.

Statistical analysis

All the experiments were carried out with three samples per each group. Statistical analysis was conducted by Statistical package for the social sciences (SPSS 23, SPSS Inc., USA). All experimental data were converted to mean \pm standard deviation. Normality of the variables was assessed using the Shapiro–Wilk test, and the statistical analysis was conducted by one-way analysis of variance (ANOVA) followed by Tukey’s post-hoc comparison. A p -value < 0.05 was deemed significant.

2.3. Results and discussion

Surface characterization

The surface and cross-sectional morphologies of the Fe substrate before and after TIPS treatment were investigated with a FE-SEM, FIB, and STEM (**Fig. 1**). TIPS treatment leads to the obvious change in surface feature of the Fe substrate; smooth surface morphology of the bare Fe with several polishing marks completely disappears after the treatment, and homogeneous nanostructures are created over the Fe surface (**Figs. 2.1a–d**). From the low-magnification image, the Fe substrate still possesses macro- and micro-scale surface flatness after the TIPS treatment, but the high-magnification and cross-sectional images reveal that the well-organized nanoridges are strongly adhered to the Fe substrate with average height, width, and gap of 345 ± 18 nm, 200 ± 18 nm, and 102 ± 10 nm, respectively. There are no signs of physical interface between the surface nanostructure and substrate. The STEM and EDS mapping images clearly show the cross-sectional elemental distributions for major elements, Ta and Fe, after the TIPS treatment; the implanted Ta are mostly distributed at the top region of the nanoridges, whereas the bottom region appears to be composed of bare Fe without Ta (**Fig. 2.1e**). From the EDS analysis at three different spots in **Fig. 2.1e** (p1: top, p2: middle, and p3: bottom), the highest atomic concentration of Ta appears only ~ 50 at% at the top of the nanoridged surface, which gradually decreases towards the bottom of the

nanoridges to 0 at%. Based on its morphology and elemental composition, the Fe substrate after TIPS treatment was defined as the nano Ta-Fe, while the untreated Fe was named as the bare Fe (**Fig. 2.1f**). Even though the Fe is well-known for its promising mechanical strength and potential as biodegradable implants, there is a current limitation when this material is treated for orthopedic injury due to its extremely slow degradation rate. In addition, in physiological environment, deep and narrow local degradation zones formed on the surface of Fe may lead to the significant deterioration of its comprehensive mechanical performances, thereby resulting in unexpected mechanical failure of the Fe implant before completing bone healing process. In this study, to address this issue, we developed the novel combination of nanostructured surface topography and galvanic reaction for achieving the uniform and accelerated degradation behavior of the Fe implant. As the nanostructured surface possesses an extremely large surface area to volume ratio, this combination could substantially increase the contact surfaces between the Fe implant and corrosive body fluids, and thereby effectively enhance the degradation rate of the Fe implant. In addition, nanostructured surfaces have dimensional similarity to those of components of extracellular matrix, which offers unique ability to directly influence the cellular and molecular events on the implant surface. In order to develop the nanostructured surface galvanic pairs on the Fe substrate, we employed the recently developed TIPS technique with noble Ta as a source of ion implantation. The TIPS

technique enables to generate numerous positive Ta ions from the Ta sputtering gun, and subsequently implant them onto the negatively charged surface of Fe substrate by applying the substrate bias. As shown in **Fig. 2.9**, the degree of applied negative bias voltages to the Fe substrate determined the variation of surface roughness of the Fe substrate due to the influence of incident Ta ion energy and surface erosion rate of Fe substrate. Under applying low-negative substrate bias voltages (≤ 500 V), incoming Ta ions had insufficient kinetic energy to sputter the Fe substrate, and the dense and crack-free Ta coatings were merely formed on the surface of Fe substrate. On the contrary, with an applied bias voltage of -1000 V, Ta ions were strongly accelerated by the sheath electric field and impact on the top surface of the Fe substrate, resulting in the continuous surface erosion of the Fe substrate rather than deposition. Under extremely high-negative substrate bias voltage (≤ 1500 V), it was confirmed that the Fe surface exhibited uneven structural collapse rather than forming nanostructures due to too strong ion bombardment. More importantly, as shown in the cross-sectional STEM images of the surface (**Fig. 2.1e**), the Ta element was inhomogeneously implanted into the Fe surface, which is considered as the reason of local surface erosion rate differences, and thereby development of surface nanostructures. Because of this unique characteristic of the TIPS technique, the nanostructured surface layer could possess excellent structural continuity and integrity with the Fe substrate without any visible physical interface. In addition, a considerable amount of Ta element (< 50 atom%) was

stably implanted in the upper region of the surface nanostructure, indicating that it should achieve mechanically robust Ta-Fe nano-galvanic pairs (**Fig. 2.1f**).

Degradation Property

The electrochemical behaviors of bare Fe and nano Ta-Fe were investigated using SKP, potentiodynamic polarization, and EIS analysis (**Fig. 2.2**). The electrochemical parameters calculated by Tafel extrapolation from potentiodynamic polarization curves are listed in **Table 1.1**. **Figs. 2.2a and b** shows the map of surface potential distribution obtained by SKP measurement from the bare Fe and nano Ta-Fe samples. Nearly uniform distribution of surface potential is observed for both samples, but the development of nanoridges surface with Ta implantation leads to a decrease of average surface potential from -491 mV to -573 mV. This trend is also seen in the result of potentiodynamic polarization analysis (**Figs. 2.2c-d** and **Table 1.1**). The anodic region of polarization curve (above the E_{corr}) is related to the dissolution of the Fe in the SBF solution, while the cathodic region (below the E_{corr}) represented the cathodic evolution of hydrogen gas. After TIPS treatment, the E_{corr} of the nano Ta-Fe is shifted towards more negative (active) potential values by -26 mV, while corrosion current density (I_{corr}) increases from 4.92 to $13.84 \mu\text{A} \cdot \text{cm}^{-2}$ compared to that for bare Fe. The degradation rate of Fe appears to be accelerated by the development of nanoridged surface with Ta implantation,

showing 281.3% higher average degradation rate ($\text{mm}\cdot\text{year}^{-1}$) for the nano Ta-Fe when compared with the bare Fe (**Table 1.1**). **Figs. 2.2c-d** shows the results of EIS analysis in the Nyquist representation. In the Nyquist plots, both the bare Fe and nano Ta-Fe samples exhibit a semicircle in the high-to-medium frequency region, followed by a straight line with a 45° phase angle in the low frequency range. In general, the semicircular portion of the Nyquist plot is directly corresponded to an electron transfer limited process at the metal surface/solution interface, and its diameter represents the electron transfer resistance of the corrosion process. By comparing the Nyquist plots of bare Fe and nano Ta-Fe, it was clear that the electron transfer resistance is substantially decreased after the TIPS treatment, which indicates that the nanoridged surface with Ta implantation effectively accelerates the corrosion rate of Fe substrate.

In order to investigate *in vitro* degradation behaviors of bare Fe and nano Ta-Fe, both samples were immersed in SBF solution, and their surface morphologies, concentration of Fe ion release, and degradation thickness at day 1, 14, and 28 of immersion are shown in **Fig. 2.3**. In case of the bare Fe, there is no substantial changes in the surface morphology up to 28 days of immersion; most of the surfaces are apparently flat, smooth, and clear over the testing period, while tiny degradation pits appear at day 14, and few of them grows quickly, forming broad and deep craters on the surface at day 28. On the contrary, the nano Ta-Fe undergoes dramatic morphological changes during the

immersion test. At 1 day of immersion, surface degradation features appearing as small specks were formed on the surface of nano Ta-Fe, and its appearance becomes more and more rough and irregular along with the increasing of immersion time. After 28 days of immersion, the surface of nano Ta-Fe was uniformly roughened without any sign of severe local degradation. High-magnified surface and cross-sectional images reveal that these roughened surface features are due to the formation and propagation of cracks on the nanostructured surface layer of nano Ta-Fe. Up to day 1 of immersion, the nano Ta-Fe possesses its distinct nano-roughened surface features, and there are no visible morphological changes compared with before. However, after 14 days of immersion, the nanostructured surface layer was cracked, and a cross-sectional narrow gap of sub-micron size appears between the nanostructured surface layer and the Fe substrate as a result of preferential degradations of the Fe substrate. With continuous immersion, the surface cracks were propagated and broadened, leaving the underlying Fe substrate partially visible at day 28 of immersion. Even though large cracks were formed on the surface of nano Ta-Fe, the nanostructured surface is not fully delaminated, still preserving close contacts with the Fe substrate in the cross-sectional observation. In addition, it is noteworthy that there is no deep or narrow degradation pits on the Fe surface regardless of immersion time and degree of degradation.

In the order to investigate the *in vitro* degradation rate of the samples, the

thickness of degradation byproduct, degradation depth of Fe substrate, and amount of released Fe ions from the bare Fe and nano Ta-Fe samples were also measured up to 28 days under the SBF immersion condition. As shown in **Figs. 2.3B–D**, it was clear that the degradation rate of the Fe has been significantly increased by the development of nanostructured surface layer with Ta implantation. Even though bare Fe has large variations in maximum and minimum thickness of degradation byproduct and average degradation depth of Fe substrate due to its localized surface degradation behaviors, the nano Ta-Fe presents higher values for both the thickness of degradation byproducts and depth of Fe substrate degradation and narrower value ranges than those of the bare Fe over the whole measurement period (**Figs. 2.3B and C**). This tendency also appears in the result of Fe ion release test (**Fig. 2.3D**). The bare Fe slowly released Fe ions along with the increasing of immersion time, reaching 21.6 $\mu\text{g/ml}$ of ion concentration at day 28 of immersion. On the other hand, the nano Ta-Fe demonstrated significantly enhanced degradation rate compared with the bare Fe; Fe ions are much more rapidly released from the surface of nano Ta-Fe, resulting in two times higher concentration of Fe ions for the overall immersion time; the amount of Fe ion at day 28 of immersion is 59.9 $\mu\text{g/ml}$, which is 236 % higher than that of the bare Fe. In terms of electrochemical activity, Fe is more active than Ta [55] and Ta_2O_5 [56, 57]. As a result, when the nano Ta-Fe sample is in contact with aqueous environments, its nanostructured surface involves the setting-up of electrochemical nano-galvanic corrosion cells

and becomes an excellent starting point for the uniform surface degradation with no preferential sites. Since their dimensions are in the nanometer ranges with well-defined surface pattern gaps, it makes it possible to achieve not only homogeneous increase of overall Fe surface potential (**Figs. 2.2a and b**), but also very high surface area for the aqueous environment-substrate contact within a small Fe substrate area. This should be a key factor in the accelerated and uniform surface degradation behavior of the nano Ta-Fe sample as compared to the bare Fe. According to electrochemical and immersion tests (**Figs. 2.2c–d and 2.3**), the bare Fe exhibited relatively inactive surface compared to the nano Ta-Fe, and most of the surface possessed its initial flat and smooth surface morphology during the entire immersion period. This clearly indicates the formation of close and intimate adhesion between the degradation product layer and the Fe substrate, thereby providing a stable physical barrier in enhancing the corrosion resistance and reducing the Fe surface degradation. In contrast, the nano Ta-Fe surfaces could provide only limited area (top of the surface nanostructures) at the interface; underneath the degradation product, the surface nanostructures lead to continuous access to the aqueous environment and long-lasting electrochemical activity.

Mechanical property

Mechanical properties are one of the most important factors for load-

bearing biodegradable implants. In particular, in order to provide mechanically safe and reliable supports to damaged bone tissues, they should have enough strength, structural rigidity, and flexibility during the bone healing period. Therefore, long-term mechanical durability of the bare Fe and nano Ta-Fe was tested here under the SBF immersion condition up to 40 weeks. **Fig. 2.4A** describes optical images of mechanical testing samples before and after immersion at week 12 and 40. Localized degradation regions are obviously observed on the surface of bare Fe with different contrast as light gray dots at week 12 of immersion, and with increasing immersion time, its surface became markedly rough, and deep craters were randomly distributed on the surface. In contrast, the nano Ta-Fe appears to be relatively uniform in color and texture over its entire surface, and no significant change or abnormality in appearance is observed with time. On the other hand, as shown in **Fig. 2.4Ba**, the result of thickness loss clearly indicates the progressive and rapid degradation behavior of the nano Ta-Fe despite its less morphological changes compared to the bare Fe. During the whole period of immersion, the nano Ta-Fe shows the higher levels of thickness loss than the bare Fe, and the differences between them become more pronounced with immersion time.

The mechanical behaviors of the bare Fe and nano Ta-Fe samples were evaluated by tensile tests before and after immersion for 12 and 40 weeks. Typical tensile stress–strain curves of each sample are shown in **Fig. 2.4Bb**. All

the curves exhibit steep initial linear slopes in the elastic region and gradual increases of the stress with deformation in the plastic region, followed by ductile failure behaviors after reaching their ultimate tensile strength (UTS). Even though the bare Fe and nano Ta-Fe samples have almost identical curve shapes before the immersion test, only the bare Fe exhibits substantial loss of mechanical properties as the immersion time increases. As shown in **Figs. 2.4Bc and d**, the UTS and elongation rate of the bare Fe gradually decrease with immersion time, showing 32% and 25% loss of UTS and elongation rate at week 40 than those before immersion, respectively, while the nano Ta-Fe has almost the same values with no statistical differences. The differences of UTS and elongation rate between the bare Fe and nano Ta-Fe samples become more pronounced with immersion time.

Since the localized surface degradation has significant relationship on rapid deterioration of the mechanical properties of the implant, the gradual changes of the surface morphology with immersion time are also represented by 3D images in **Fig. 2.4C**, and their detail surface roughness values (R_a : arithmetic mean deviation, R_q : root mean square deviation, R_p : maximum profile peak height, and R_v : maximum profile valley height) are listed in **Table 1.2**. In case of the bare Fe, there is substantial changes in the surface morphology up to 40 weeks of immersion; flat and smooth surface of the bare Fe completely turns into rough and irregular with deep and wide dimples distributed all over the

surface at week 12, which becomes more prominent at week 40. On the contrary, the surface of nano Ta-Fe appears to be more uniformly corroded and nearly flat up to 12 weeks of immersion. Although it also shows micro-scale roughened surface at week 40, only shallow craters are sparsely distributed, and its average surface roughness (R_a and R_q) and maximum peak (R_p) and valley heights (R_v) are almost three times lower than those of the bare Fe. *In vitro* mechanical and *in vivo* degradation assessments verified that the surface nanogalvanic corrosion cells of the nano Ta-Fe enabled the uniform surface degradation and consistence mechanical performance within 40 weeks. In case of the bare Fe, under the body fluid exposure, localized surface degradation of Fe can be randomly initiated by the competitive adsorption between chloride ions and the passive species (such as hydroxide ions and dipoles of water molecules) [58]. Once the concentration of chloride ions reached to a critical value on the surface of Fe substrate, it can allow to initiate and propagate the local Fe degradation over a long period of time, which in turn produced readily observable deep and irregular craters on the surface of Fe substrate (**Figs. 2.6C** (in vitro) and **2.7A** (in vivo)). This behavior is regarded as one of the most destructive and insidious metal degradation types and directly affected not only strength, but also ductility of the implant. The presence of surface irregularities easily leads to stress concentration in the deep and narrow crater regions under physiological load conditions that could subsequently trigger the uncontrollable propagation of cracks at lower strain and stress levels than in a uniform surface.

Since design, manufacturing, and assessment of orthopedic implants are generally based on an assurance of consistent mechanical performance after implantation, the bare Fe could no longer be regarded as acceptable and safe for use in clinical practice. On the contrary, in case of the nano Ta-Fe sample, numerous nano-galvanic cells formed on its surface are crucial to the enhancement of surface degradation activity and resulted in uniformly distributed degradation sites with a significant reduction of surface roughness both *in vitro* and *in vivo*. Therefore, although its relatively higher volumetric loss than the bare Fe sample, the nano Ta-Fe could exhibit almost unchanged values of UTS and elongation rate up to 40 weeks of immersion. These long-term statistical results imply that the nano Ta-Fe implant can be regarded as a long-term reliable and stable treatment option in clinical practice.

***In vitro* cellular response**

Wettability is one of the most important surface properties of an orthopedic implant affecting cell–implant interaction and bone tissue responses. Therefore, prior to investigating cellular responses, water contact angle formed on the bare Fe and nano Ta-Fe samples was measured (**Fig. 2.5A**). Compared to the bare Fe, the nano Ta-Fe exhibited substantially enhanced surface hydrophilicity, as shown in Fig. 5A; the angle of the water droplet was nearly spread out on nano Ta-Fe surface, showing contact angle of 15°, while the bare

Fe shows a near hydrophobic surface (contact angle $\approx 55^\circ$).

For *in vitro* biocompatibility evaluation of the bare Fe and nano Ta-Fe, the response of osteoblasts (MC3T3) to both samples was closely examined in terms of cell adhesion morphology and viability. **Fig. 2.5B** shows CLSM and FE-SEM images of the samples after 6, 24, and 72 h culturing, from which the cells have a more pronounced morphological response to the surface of nano Ta-Fe than those to the bare Fe for all time points. On the surface of nano Ta-Fe, cells are tightly adherent and spread extensively, causing closer cell–cell interactions and better cell surface coverage than the bare Fe only after 24 h of incubation. In addition, a higher number of filopodia-like cell protrusions are produced at the spreading edge of the cells on the nano Ta-Fe compared to the bare Fe. The multiple small protrusive structures (indicated by arrows) are extending from the cell and anchor to the top of the surface nanostructures, leading to a proper extension of cell surfaces, whereas the cells on the bare Fe forms a single needle-like (long and narrow) cell protrusion. After 72 h culturing, even though both samples are found to have substantial amounts of degradation byproducts, covering a large portion of cell surfaces, the cells preserve their integrity and viability without noticeable adhesion shape change or detachment from both surfaces.

In order to further investigate the effect of degradation byproducts, especially ionic products (Fe^{2+} and Fe^{3+}), on the osteoblasts viability, the cells

were cultured up to 3 days in the culturing media obtained after 2 days of incubation with bare Fe and nano Ta-Fe samples (**Fig. 2.5C**). For references, culturing media containing 10% FBS or 10% DMSO were also included in this measurement as a positive or negative control, respectively. After 1 day of culturing, the bare Fe and nano Ta-Fe samples exhibit no cytotoxicity signs to osteoblasts; their cell viability levels are almost identical to the positive control without any statistical significance (vs. bare Fe: $p = 0.741$, and vs. nano Ta-Fe: $p = 0.552$). Even though they showed somewhat lower levels of cell viability than the positive control after 3 days of culturing, the cells in the culturing media obtained with bare Fe and nano Ta-Fe samples also significantly proliferated almost 3 times between days 1 and 3, while the negative control shows negligible levels of cell viability in all time points.

The blood compatibility of the bare Fe and nano Ta-Fe was also confirmed by the result obtained from material-induced platelet adhesion and aggregation test, which is regarded as an important factor influencing the outcome of medical implant and its success. After incubation of the samples into platelet-rich plasma solutions for 45 min, the adhered platelet morphology and its numbers on the surface of bare Fe and nano Ta-Fe are demonstrated in **Figs. 2.5D** and **E**. In low-magnified FE-SEM image, a large number of platelets adhered to and locally aggregated on the surface of bare Fe, and their morphologies are noticeably changed into irregular central bodies with multiple

long dendritic pseudopodia at the adhesive points in high-magnified image. On the contrary, the number of adhered platelets on the nano Ta-Fe surface is apparently reduced, and they still retain their original spherical shape with nearly no formation of pseudopods. As shown in **Fig. 2.5E**, the nano Ta-Fe exhibits 34% fewer density of adhered platelets with statistical significant ($p < 0.05$) when compared with bare Fe. Biocompatibility of the bare Fe and the nano Ta-Fe samples was confirmed by both *in vitro* cellular response and *in vivo* animal tests. Even though Fe element participates in a wide variety of metabolic processes in the body, when the level of released Fe ions from the implant exceed a tolerable limit for the uptake by intracellular elements, cells inevitably suffer various degree of cytotoxicity, and severe immunogenic responses can be triggered, thereby limiting its efficacy and biosafety [59]. In fact, as shown in **Figs. 2.3D**, and **2.7B**, the nano Ta-Fe exhibited almost two times higher amount of Fe ion release than the bare Fe implant in SBF immersion test, and after implantation into the rabbit femur medullary cavity, the Fe ions were broadly distributed in the bone marrow tissue around the nano Ta-Fe implant, as compared to the bare Fe. Therefore, in order to eliminate such a concern, we performed two different sets of *in vitro* assay in which the osteoblasts were cultured on either the sample surfaces directly with fresh culturing media (case 1) or the culture plates with culturing media obtained after pre-incubation with bare Fe and nano Ta-Fe samples (case 2). The result of case 1 assay clearly reveals that the nano Ta-Fe provided the favorable

surface environments for cell attachment and spreading, showing the higher number of adhered osteoblasts on its surface with wider spreading morphologies than those on the bare Fe (**Fig. 2.5B**). In addition, the osteoblasts proliferated significantly almost three times from day 1 to 3 with no difference of cell viability between the bare Fe and the nano Ta-Fe samples at any culturing time point in the case 2 assay (**Fig. 2.5C**). It is proved that the extremely high concentrations of Fe ions (≥ 170 mg/ml) lead to the oxidative damage to lipids, suppressed mitochondria activity, and the formation of large precipitates in cytoplasm, thereby inducing severe cell damages. In this study, the accumulated Fe ion concentrations up to 28 days for the bare Fe and the nano Ta-Fe samples were only 21.6 $\mu\text{g/ml}$ and 59.9 $\mu\text{g/ml}$, respectively, which is apparently in the range of biologically acceptable tolerance. This *in vitro* assay is well matched with the *in vivo* immunohistological analysis where the nano Ta-Fe implant did not show any sign of local toxicity compared to the pure Fe implant (**Fig. 2.7C**). In addition, our previous studies showed that the nanostructured surfaces, such as pores, wells, and grooves, were able to elicit biologically active cellular responses by regulating integrin-dependent cell adhesion signaling pathways. In particular, surface features in the size range 200–300 nm have shown a profound effect on the surface hydrophilicity and formation of focal adhesion and filopodia extension of cells, leading to a considerable extension of cell structure. During this process, filopodia plays an essential and primary role in signaling and sensing surrounding microenvironment and stabilizing of the

cytoskeleton structure of cells on the top of the surface nanostructures. Therefore, the formation of numerous filopodia-like cell extrusions and enhanced cell spreading behaviors of osteoblasts on the nano Ta-Fe clearly represent active cell-surface interaction, thereby increasing the possibility of producing intimate implant contact with the host bone tissue. The substantially improved surface hydrophilicity of the nano Ta-Fe also provided high affinity to the blood by preventing platelet adhesion and activation on its surface. Since the hydrophobic surfaces lead to the strong adsorption and irreversible conformational change of blood proteins via hydrophobic interaction, the hydrophilic surface property of the nano Ta-Fe could prevent protein denaturation and suppress subsequent platelet recruitment, adhesion, and activation (**Figs. 2.5D and E**).

***In vivo* degradation analysis**

To evaluate the *in vivo* degradation rate of the materials, cylindrical shaped bare Fe and nano Ta-Fe implants were inserted into each side of the femoral bone marrow cavity for a rabbit, and after 4 and 16 weeks, 3D volumetric and 2D cross-sectional surface morphometric analysis were performed by micro-CT and FE-SEM/EDS. As shown in **Fig. 2.6A**, in the 3D images of the inserted implants with bone tissue and their 2D coronal and transverse images (without bone tissue), both implants appear to have uniform

and regular surface morphologies with no macroscopic deformations or damages over large surface areas up to week 16 after implantation. In addition, there are no indications of bone erosion or resorption around both implants during the observation period. The quantitative residual volume of the implants was measured by the micro-CT before and after implantation at weeks 4 and 16 (**Fig. 2.6B**). Obviously, under the *in vivo* circumstance, the nano Ta-Fe implant lost its volume at a faster rate than the bare Fe, showing 211 % faster average volumetric loss value compared to the bare Fe from initial volume to weeks 16.

In addition, high-magnified FE-SEM images clearly show the localized biodegradation behavior of the bare Fe implant; a narrow and deep pit is formed on the surface of bare Fe at week 4, and it gets further broadened with increasing implantation period (the blue rectangle regions in **Fig. 2.6C**). Even though the nano Ta-Fe implant also exhibits roughened surface topography, only small-scale roughness features appear without any deep or localized pitting on its surface during the whole implantation period. In EDS mapping results, the thin and uniform distribution of oxygen element, a possible degradation product from the Fe substrate, is clearly observed on the surface of nano Ta-Fe, whereas it is locally and severely accumulated only nearby the surface pit or deep crater on the surface of bare Fe.

***In vivo* histological and immunohistochemical analysis**

Histological and immunohistochemical images of the bare Fe and nano Ta-Fe implants after implantation at weeks 4 and 16 are shown in **Figs. 2.7A–C**. The transverse sectioned implants were stained with H&E and Prussian blue, and the expression of macrophage was detected through CD68 immunostaining. As shown in **Fig. 2.7A**, the bare Fe implant exhibited the non-uniform surface degradation behaviors. After 4 weeks of implantation, the surface of bare Fe in the blue rectangle region becomes significantly rough, and degradation byproducts surround its surface, representing brownish color in high magnification H&E image, whereas there were no noticeable morphological changes in the red rectangle region. As the implantation period progressed, the bare Fe still exhibits rough and irregular surface morphology, and a significant amount of degradation byproduct are generated only in the blue rectangle region. In contrast, in case of nano Ta-Fe implant, the uniform surface morphological change can be seen with increasing implantation time; in both the blue and red rectangle regions, the nano Ta-Fe appears to retain smooth surface morphology after 4 weeks of implantation, and it is not noticeably changed when the implantation further progressed up to week 16.

The presence of Fe ions in the surrounding bone marrow tissues are confirmed by Prussian blue staining, in which ferric ions (Fe^{3+}), oxidized form of Fe degradation byproduct, in the tissue appears to be in blue, as shown in **Fig. 2.7B**. After 4 weeks of implantation, the bare Fe implant exhibits only

negligible Fe^{3+} ion penetration into the surrounding tissue; at low and high magnified images, almost all tissues are stained in red, and it was hard to identify the specific penetration depth of Fe^{3+} ions into the bone marrow tissue. In case of the nano Ta-Fe implant, its low-magnified stained image seems to be similar to that of the bare Fe at week 4 of implantation. However, with high magnification, the light-blue stained region is clearly observed, and its thickness appears relatively constant with average thickness $56.8 \pm 6.3 \mu\text{m}$. As the implantation period increases, the nano Ta-Fe sample shows more pronounced, widespread Fe^{3+} ion penetration in the bone marrow tissue; even at low-magnified image, the Fe^{3+} ion penetrated regions are easily observable around the nano Ta-Fe sample, and it appears to be in relatively uniform distribution with average thickness $131.0 \pm 18.0 \mu\text{m}$. Although the bare Fe also exhibit significant increase of average ion penetration depth from $18.5 \pm 13.7 \mu\text{m}$ to $113.1 \pm 68.4 \mu\text{m}$ from week 4 to 16 of implantation, there is marked inhomogeneity along the inner surface of the bone marrow tissue, and no blue-stained tissues are still observed.

In order to investigate the immune responses, the expression of macrophage in the bone marrow tissue was detected by immunohistochemical staining for CD68 marker; this is known to play a predominant role in foreign body reaction, acute/chronic inflammation, and implant loosening [60]. As shown in **Fig. 2.7C**, at week 4 of implantation, both the bare Fe and nano Ta-

Fe present a few number of brown-stained CD68-positive macrophages in the bone marrow tissue, and their numbers significantly increase with increasing implantation time up to 16 weeks. Even though the nano Ta-Fe shows slightly lower average macrophage numbers than the bare Fe at weeks 4 and 16, but there are no statistical differences between them ($p = 0.732$ at week 4 and $p = 0.909$ at week 16, respectively).

2.4. Conclusion

A novel strategy to accelerate the degradation rate of Fe implant with uniform surface degradation behavior has been demonstrated using the TIPS surface modification technique. In this technique, numerous Ta ions were generated and accelerated strongly toward the surface of Fe implant under the applied high negative bias voltage to the Fe implant, which makes it possible to develop Ta-implanted nanostructures on the Fe implant surface via continuous Fe surface erosion. Because of the relatively higher corrosion potential of Ta than the Fe, the surface of nano Ta-Fe acts as effective nanogalvanic couples under body fluid conditions and leads to increased rate of surface corrosion. Although the relatively high degradation rate of the nano Ta-Fe, its uniform surface degradation behavior makes it possible to possess almost consistent mechanical properties up to 40 weeks of immersion. The *in vitro* osteoblast assay and *in vivo* rabbit femur medullary cavity implantation confirmed that the nano Ta-Fe enhanced the osteoblasts adhering and spreading on the surface, and there is no sign of cellular and tissue toxicity, despite its high level of release Fe ions as compared to the bare Fe implant. The present study demonstrates that the TIPS technique will offer a new and safe approach in the pretreatment of Fe orthopedic implants to achieve the accelerated degradation rate and enhance the clinical outcome and biosafety of the implant.

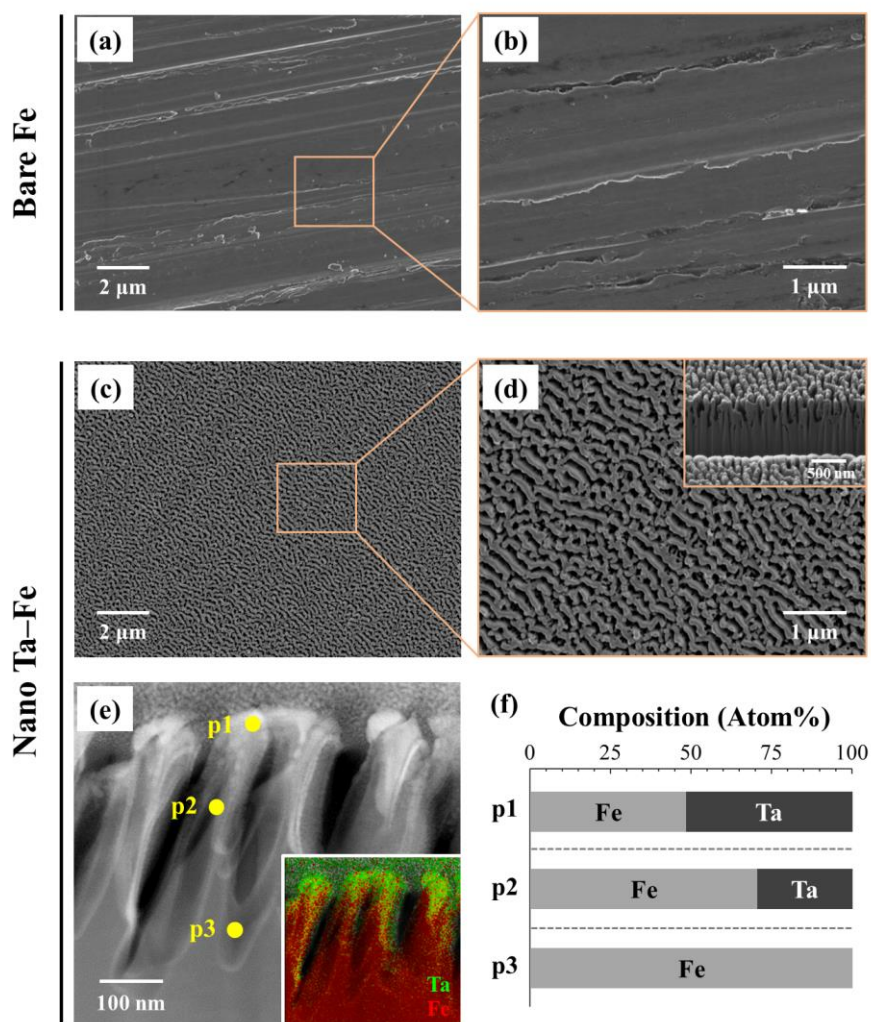


Figure 2.1. Representative surface field-emission scanning electron microscopy (FE-SEM) images of (a), (b) bare Fe and (c), (d) nano Ta-Fe at low and high magnification. The inset in (d) displays the cross-sectional focused ion beam (FIB)/FE-SEM image of the surface of nano Ta-Fe. (e) Cross-sectional scanning transmission electron microscopy image of nano Ta-Fe with energy-dispersive X-ray spectroscopy mapping (inset), and (f) chemical compositions at three regions in e (p1: top, p2: middle, and p3: bottom).

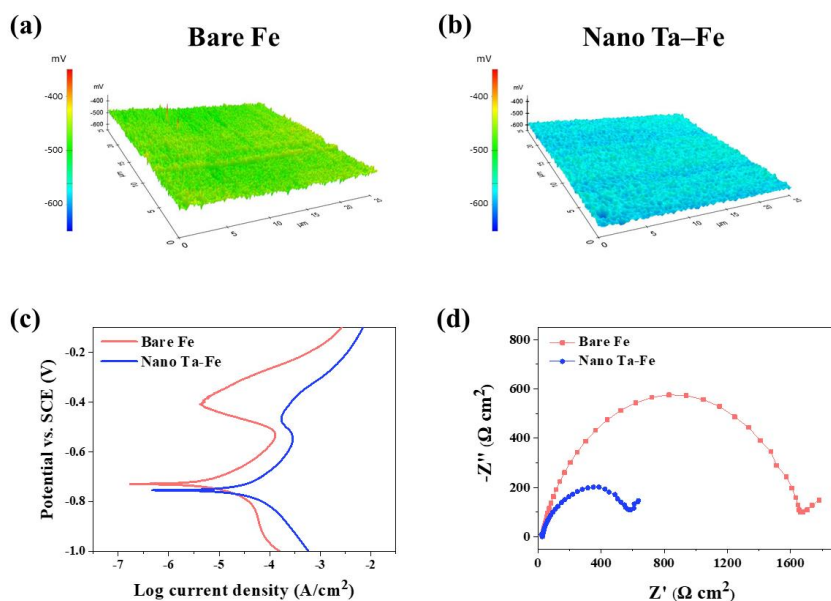


Figure 2.2. Electrochemical corrosion behaviors: Scanning Kelvin Probe maps of (a) bare Fe, (b) nano Ta–Fe, (c) Potentiodynamic polarization curves, and (d) Nyquist plots.

Sample	E_{corr} (V)	I_{corr} ($\mu\text{A}\cdot\text{cm}^{-2}$)	Degradation rate ($\text{mm}\cdot\text{year}^{-1}$)
Bare Fe	-0.728	4.920	0.057
Nano Ta-Fe	-0.754	13.836	0.161

Table 1.1. Electrochemical degradation properties of bare Fe and nano Ta-Fe samples.

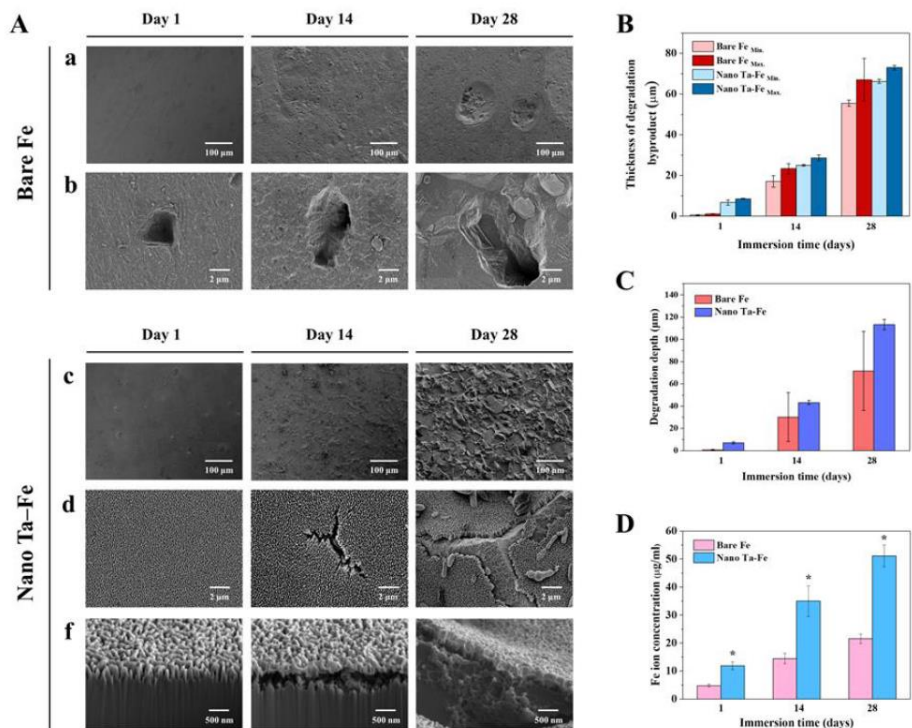


Figure 2.3. *In vitro* degradation test for 28 days in simulated body fluid solution to observe the degradation pit formation and degradation rate. (A) Field-emission scanning electron microscopy (FE-SEM) images of surface morphology of bare Fe and nano Ta-Fe at (a), (c) low magnification and (b), (d) high magnification, and (f) cross-sectional focused ion beam (FIB)/FE-SEM image of nano Ta-Fe. (B) Thickness of degradation byproducts (abbreviations Min. and Max. denote the minimum and maximum thickness, respectively, of the degradation byproducts). (C) Degradation depth of bare Fe and nano Ta-Fe. (D) Released Fe ion concentration of bare Fe and nano Ta-Fe.

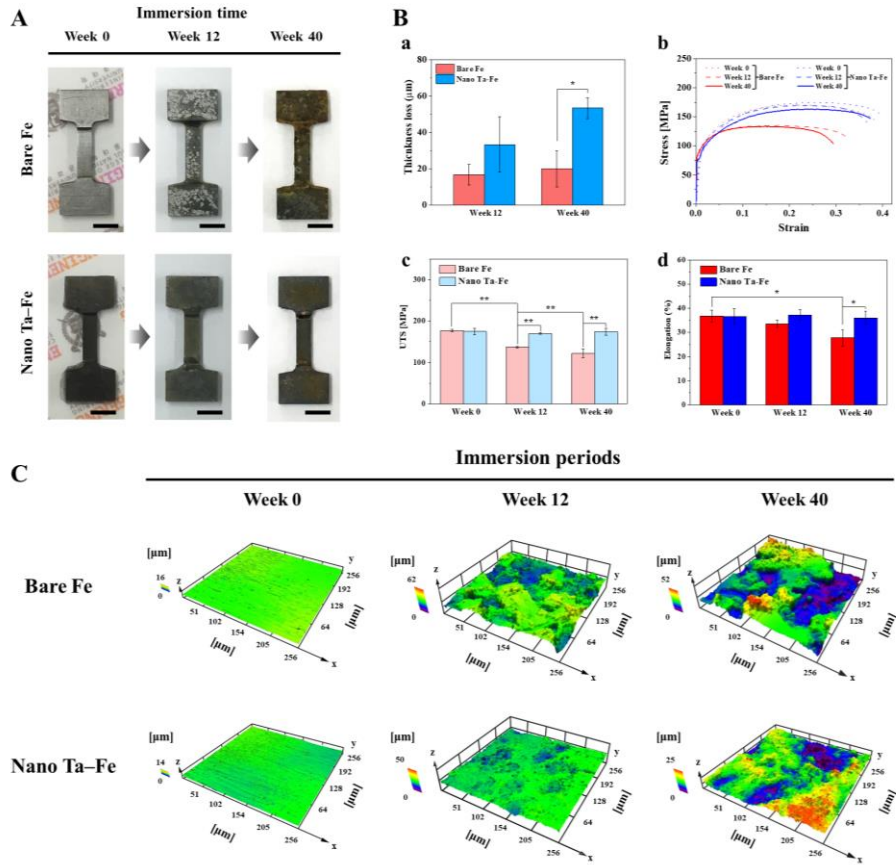


Figure 2.4. (A) Optical images of bare Fe and nano Ta-Fe before and after 12 and 40 weeks of immersion in simulated body fluid solution. The inset scale bar is 500 μm . (B) Tensile tests of bare Fe and nano Ta-Fe up to 40 weeks of immersion; (a) thickness loss, (b) stress–strain curves, (c) ultimate tensile strength, and (d) elongation rate (*: $p < 0.05$ and **: $p < 0.005$). (C) Three-dimensional surface topography as a function of immersion period using a laser scanning microscope.

	Bare Fe			Nano Ta–Fe		
	Week 0	Week 12	Week 40	Week 0	Week 12	Week 40
R_a (μm)	0.430 ± 0.075	0.479 ± 0.052	4.059 ± 0.946	0.371 ± 0.056	0.369 ± 0.043	1.454 ± 0.135
R_q (μm)	0.555 ± 0.077	0.642 ± 0.067	4.929 ± 1.145	0.581 ± 0.109	0.478 ± 0.054	1.840 ± 0.190
R_p (μm)	1.493 ± 0.375	2.510 ± 0.373	9.087 ± 1.582	1.138 ± 0.116	1.517 ± 0.216	3.260 ± 1.234
R_v (μm)	2.146 ± 0.503	2.602 ± 0.332	11.149 ± 4.260	1.588 ± 0.106	1.706 ± 0.438	4.077 ± 1.423

Table 1.2. Surface roughness parameters of bare Fe and nano Ta–Fe up to 40 weeks of immersion in simulated body fluid solutions.

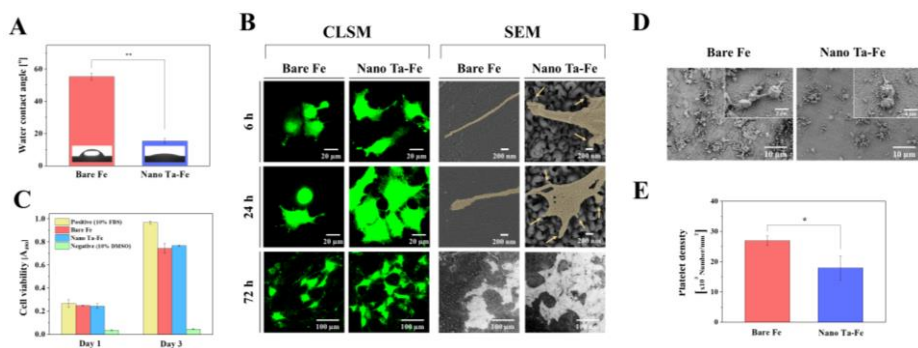


Figure 2.5. (A) Water contact angles of bare Fe and nano Ta-Fe. (B) Low-magnification confocal laser scanning microscopy and high-magnification field-emission scanning electron microscopy (FE-SEM) images of attached osteoblast cells (MC3T3) on bare Fe and nano Ta-Fe surfaces after culturing for 6, 24, and 72 h. (C) Osteoblast cell viability in extracted culturing media with bare Fe and nano Ta-Fe immersions. (D) Representative FE-SEM images of adhered platelets on the surface of bare Fe and nano Ta-Fe. (E) Adhered platelet density on the bare Fe and nano Ta-Fe surface. (*: $p < 0.05$ and **: $p < 0.005$)

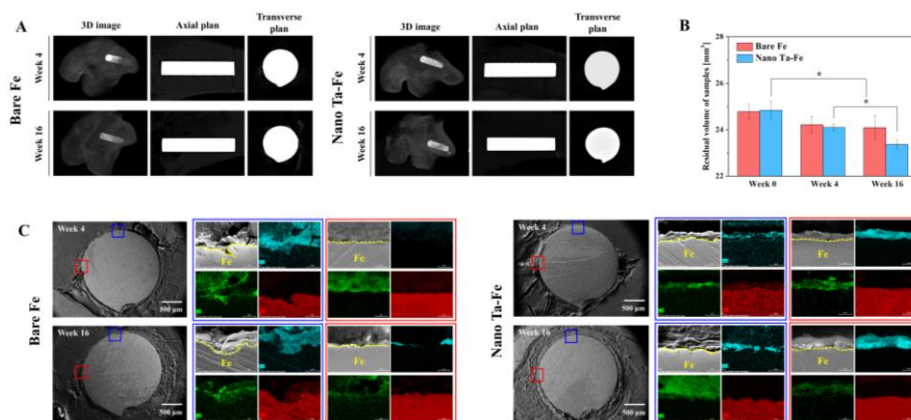


Figure 2.6. (A) Three-dimensional (3D) reconstruction images of micro-computed tomography scans after 4 and 16 weeks of *in vivo* experiments. (B) Residual volume of bare Fe and nano Ta-Fe after 4 and 16 weeks. Statistical significance is indicated as * ($p < 0.05$). (C) Scanning electron microscopy images and corresponding energy-dispersive X-ray spectroscopy mapping images obtained from rectangular regions in the cross sections of bare Fe and nano Ta-Fe after 4 and 16 weeks of *in vivo* degradation testing (oxygen: light blue, iron: red, and carbon: green).

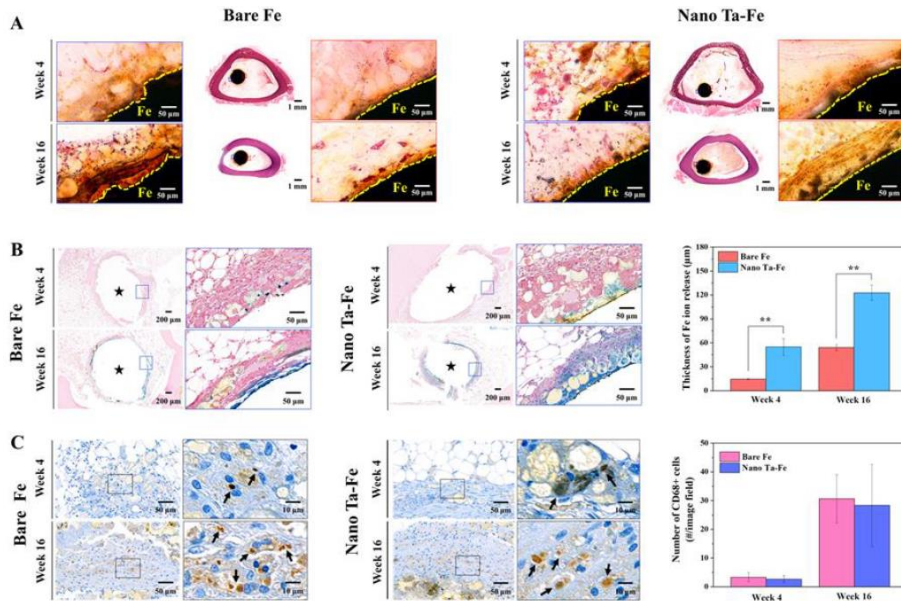


Figure 2.7. *In vivo* histological and immunohistochemical characterization of the rabbit femur bone marrow implantation study. (A) Hematoxylin–eosin (H&E), (B) Prussian blue, and (C) CD68+ stained mid-diaphyseal femoral cross sections. The average thickness of Fe ions released into the bone marrow tissue and the number of CD68+ macrophages in the bone marrow of the rabbit are presented in (B) and (C), respectively, as a function of *in vivo* implantation time. Black stars in (B) indicate the implant inserted regions. Statistical significance is indicated as ** ($p < 0.005$).



Figure 2.8. Schematic diagram of the TIPS process for Fe implants with Ta sputter target and negative substrate bias voltage of 1,000 V.

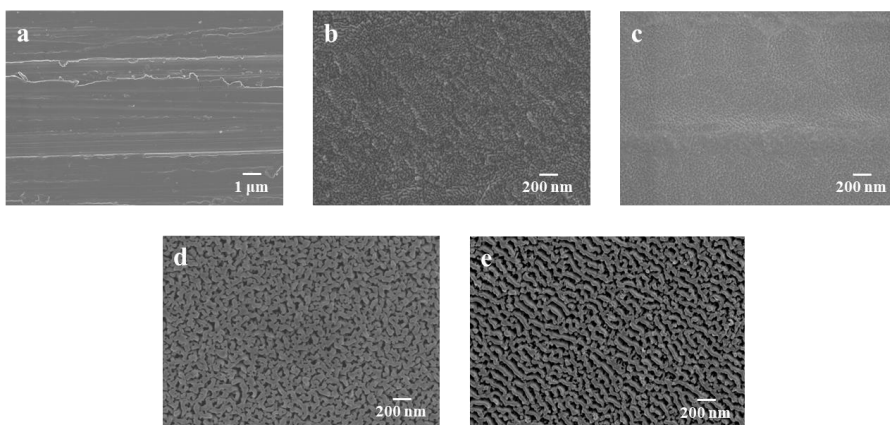


Figure 2.9. Representative surface field-emission scanning electron microscopy images of Fe samples with different negative substrate bias voltages for TIPS surface treatment: (a) 0 V, (b) 250 V, (c) 500 V, (d) 750 V and (e) 1000 V.

Chapter 3.

**Bio-inspired Cobalt-Chrome surface with both
enhanced biological activity and bactericidal effect**

3.1. Introduction

For the past decades, metal-based biomaterials have been widely used throughout the biomedical field [61-63]. The characteristics such as bio-inertness and excellent mechanical property have contributed to making metals promising materials in the field of biomaterials. Metallic bio-implant can support impaired tissue mechanically due to its excellent mechanical property. Among various metals, Titanium (Ti)- [64, 65], Iron (Fe)- [66, 67], and Cobalt (Co)-based alloys have been used [6].

Co-based alloys are one of the widely used bio-metals for soft and hard tissue regeneration and replacement such as cardiovascular, orthopedic, and dental applications. Co-Cr alloys play an excellent role as a supporter in the tissue subjected to load due to excellent mechanical strength and elasticity [44]. However, despite of these achievements, the low cytocompatibility and antibacterial property, which limit their use in medical applications. Co-Cr alloys are not rapidly assimilated with the surrounding bone tissue after implantation because of low biocompatibility leading to the implant failure. In particular, the poor antimicrobial properties of Co-Cr alloys are regarded as the main issue causing severe peri-implantitis and osteomyelitis in dental and orthopedic implant materials, respectively [68].

To overcome the poor antimicrobial properties of Co-Cr-based implant materials, the methods of incorporating antibiotics or silver coating on

the surface of implant materials have been actively studied [69, 70]. The Co-Cr implant surface incorporated with antibiotics exhibits excellent resistance to bacteria after medical implantation which is the most simple and convenient method to prevent implant failure from the bacterial infection [71]. However, it induces adverse effects including deterioration in cell viability and cell necrosis on mammalian cells [72, 73]. The silver-coating also imparts excellent antibacterial properties to Co-Cr [74]. However, as the silver content increases, it shows severe cytotoxicity on the various cells. As described above, previous research has mainly focused on containing antimicrobial agents on the surface to impart excellent antibacterial properties to metallic implants. However, it causes a fatal problem on the viability of bone cells.

It was recently suggested that the nanostructure of dragonfly wings exhibits excellent antibacterial effects itself [75, 76]. The nanostructure of the dragonfly wings has a mechano-antibacterial effect that physically damages the membrane of bacteria attached to the surface in a structure like a needle. The bacteria cell walls on the nanostructure are physically tensioned by the nanostructure, which ultimately causes the membrane to rupture. This mechano-antimicrobial effect was demonstrated in both gram-negative and positive bacteria. Therefore, it is intended to develop a multi-functional bio-implant that not only imparts antibacterial properties to the implant by imitating dragonfly wings with excellent antibacterial properties, but also improves

biocompatibility at the same time due to nano-topography. We utilized Target-ion Induced Plasma Sputtering (TIPS) process to imitate dragonfly wings [49]. TIPS is a technology that attracts attention as a promising surface treatment tool for biomaterials that forms nanostructures on the surface of metallic materials through massive ion bombardment and implantation. In this system, the metal cations emitted from the target are accelerated by an extremely high negative bias voltage applied to the substrate, thereby impinging a high impact energy on the metal substrates and colliding with it. Nanostructures having various biological functions are formed on the metal substrates by the impact of target ions [24-26]. The TIPS method has the advantage of not only physically changing the topography of the material surface, but also surface chemistry simultaneously.

In this study, we utilized the TIPS technique using tantalum (Ta) as a target material to mimic dragonfly wings, as it has a much higher biocompatibility than Co-Cr and is well-known for its favorable interaction with bone tissue. Four experimental groups Flat (Control), Ta coated, Nano-spike (Bio-inspired), and Nano-ripple Co-Cr were used to investigate the antimicrobial effect and cytocompatibility of Co-Cr before and after the treatment of TIPS. Surface structure, chemical composition analysis, antibacterial property, and biocompatibility were evaluated.

3.2. Materials and methods

Fabrication of bio-inspired Co-Cr surface

Commercial L605 Cobalt-Chrome alloy (Co-Cr) with a rectangular shape (10 mm × 10 mm × 2 mm) was processed for the surface characterization, Bacteria studies, and osteoblast cell test. All samples were ultrasonically cleaned in ethanol 10 min before the Ta ion etching and coating processes. A Ta target (75-mm diameter, 5-mm thickness, 99.99% purity, Avention, Korea) was located in a direct current (DC) magnetron sputtering gun (Ultech Co. Ltd, Daegu, Korea). Prior to the sputtering process, the vacuum chamber was sequentially pumped down to 5×10^{-4} Pa with rotary pumps followed by diffusion pumps. To generate numerous Ta ions, 65 W of target power was directly given to the Ta target. The working temperature and pressure of the process were maintained at 0.6 Pa and 25 °C, respectively. Ta coated Co-Cr surface were fabricated by sputtering without a negative substrate bias voltage to confirm the compositional effects on bacteria and osteoblast cells. TIPS was treated on bare Co-Cr surfaces with a negative substrate bias voltage (−2 kV) for 5 to 30 min to fabricate various surface morphologies. TIPS treated Co-Cr surfaces for 5, 30 min were designated by the letter Nano-spike Co-Cr and Nano-ripple Co-Cr, respectively.

Surface characterization

The surface morphological observations were performed by using field-emission scanning electron microscopy (FE-SEM; JSM-6330F, JEOL, Japan), and the compositional analysis of nano-spike Co-Cr was conducted by high-resolution scanning transmission electron microscopy (STEM; JEM-2100F, JEOL, Japan) at 200 kV. The Ta distribution profile on the Co-Cr surface was investigated by the energy-dispersive X-ray spectroscopy (EDS) with elemental spot analysis mode in STEM. The cross-sectional images of all the experimental groups were obtained by focused ion beam (FIB) milling and FE-SEM equipped (FIB/FE-SEM; AURIGA, Carl Zeiss, Germany). Three-dimensional (3D) morphologies of the samples were reconstructed by Atomic Force Microscope (AFM; NX-10, Park systems, Korea). The hydrophilicity of Flat, Ta coated, Nano-spike, and Nano-ripple Co-Cr was measured by sessile drop method with distilled water. The hydrophilicity was quantified using ImageJ software.

Bacteria studies

The Antibacterial activity depending on the surface structure was assessed with gram-negative *E. coli* (ATCC, PTA-5073, Rockville, USA) and gram-positive *S. aureus* (ATCC 6538, Rockville, USA). Both bacterial cell stocks were stored at -80 °C in a Luria-Bertani (LB) broth (BD Difco™, 244620, USA) with 50% sterile glycerol. A culturing medium with 50 µl of the

stocks of *E. coli* and *S. aureus* into 3 ml of LB medium were cultured for 15 hr. Dilution of bacteria suspension was carried out by LB medium to reach a concentration of 4×10^5 CFU/ml. After that, 1 ml of suspension was seeded and inoculated onto the surface of Flat, Ta coated, Nano-spike, and Nano-ripple Co-Cr at 37 °C for 15 hr.

Bactericidal activity on samples was assessed by LIVE/DEAD Backlight Bacterial Viability Kit (L7012, Molecular Probes, Eugene, USA). All the samples were extracted from the LB medium after 3 hr of incubation and washed out with PBS solution three times. LIVE/DEAD staining was performed using solutions with SYTO9 and propidium iodide for 20 min in darkness in room temperature. Confocal laser scanning microscope (CLSM; SP8 X, Leica, Germany). The morphologies of attached bacteria were characterized with field emission scanning electron microscopy (FE-SEM; MERLIN compact, Carl Zeiss Inc., Oberkochen, Germany). Prior to the observation, 2.5% glutaraldehyde were used to fix the bacteria on the surfaces for 10 min, followed by in graded ethanol (70, 95, and 100 %). Finally, the samples were soaked in hexamethyldisilane for 10 min and coated by using a Pt coater.

For the bacterial colony tests, the specimens were rinsed with 1 ml of PBS solution immediately after incubation, and the rinsed samples were transferred into 15 ml conical tube filled with 3 ml of fresh PBS. The tubes

containing post-incubated specimens were vigorously vortexed for 1 min to detach all the bacteria from the surfaces. The viable bacteria in the PBS were characterized after standard serial dilution and spreading on LB agar plates. Subsequently, the agar plates were incubated for 12 hr and its images were acquired by a digital camera.

Osteoblast cells response (MC3T3-E1)

The biological properties were evaluated using osteoblast cells (MC3T3, ATCC, CRL-2593, USA). The osteoblast cells were cultured in α -minimum essential medium (α -MEM; Welgene, Gyeongbuk, South Korea) supplemented with 10% fetal bovine serum and 1% penicillin-streptomycin, and incubated in a humidified incubator with 5% CO₂ at 37 °C. The *in vitro* cellular assays including cell attachment, proliferation, and differentiation were conducted on the surfaces of Flat, Ta coated, Nano-spike, and Nano-ripple Co-Cr under conditions of 5% CO₂ at 37 °C. Cells were seeded on each surface of four groups at a density of 3, 2, and 1×10^4 cells/mL for cell attachment, proliferation, and differentiation tests, respectively.

The cellular attachment on the surfaces of samples were characterized by CLSM. After 3 hr of culturing, the adhered cells were fixed by 4% paraformaldehyde (Sigma-Aldrich, USA) and washed in PBS. The rinsed samples were permeabilized with 0.1% Triton (Sigma-Aldrich, USA) in PBS

for 5 min. After blocking nonspecific binding sites using 1% bovine serum (BSA; Sigma-Aldrich, USA) in PBS for 30 min. Cell nuclei and F-actin were stained with fluorescent phalloidin (Alexa Fluor 555 phalloidin, Invitrogen, USA) and 4',6diamidino-2-phenylindole (DAPI; ProLong Gold antifade reagent with DAPI, Invitrogen, USA), respectively. The surface coverage rate of osteoblast cells on each surface of samples were measured using ImageJ software (NIH, Bethesda, MD).

The cell proliferation test was performed by a methoxyphenyl tetrazolium salt (MTS, Promega, Madison, USA) assay with 3-(4,5-dimethylthiazol-2-yl)-5-(3-carboxymethoxyphenyl)-2-(4-sulfophenyl)-2H-tetrazolium as a substrate for mitochondrial reduction. After 1,3, and 6 days of culturing, the volume of formazan product was measured at 490 nm to confirm viability of cells on the surfaces.

The cell differentiation of osteoblast cells was investigated by alkaline phosphatase (ALP) activity assay after 14 days of culturing. To accelerate the cell differentiation, β -GP of 10 mM and ascorbic acid of 50 mg/mL were added to the culture medium to induce accelerated cell differentiation after 24 hr of culturing, and the culture medium was refreshed every three days. The ALP activity was quantified by a micro reader at 405 nm (Model 550, Bio-Rad Laboratories, USA).

Osteoblast/bacteria Co-culturing

To simulate the physiological environment, co-culturing test of osteoblast cells and bacteria was performed. Flat, Ta coated, Nano-spike, and Nano-ripple Co-Cr samples were pre-infected by 1 ml of *E. coli* and *S. aureus* with concentration of 10^3 CFU/mL for 3 hr and washed with PBS three times to eliminate non-adherent bacteria from the surfaces. After pre-infection with both gram-negative and gram-positive bacteria, osteoblast cell suspension was seeded onto the Flat, Ta coated, Nano-spike, and Nano-ripple Co-Cr surfaces at a concentration of 5×10^4 cells/mL and cultured for 24 hr to trigger competition between osteoblasts and bacteria. The viability of osteoblast cells under competitive environment with bacteria were investigated using Live/Dead staining (L3224, Invitrogen, Carlsbad, USA) of osteoblast cells. The surface coverage rate of live osteoblast cells was calculated by ImageJ software tool.

Statistical analysis

All experiments were conducted with three samples per group. Statistical analysis was performed by the Statistical Package for the Social Sciences (SPSS 23, SPSS Inc., USA) software, and all experimental data were converted to mean \pm standard deviation. The normality of the variables was assessed using the Shapiro–Wilk test, and the statistical analysis was performed by one-way analysis of variance followed by Tukey’s post-hoc comparison. A

p-value of <0.05 was deemed significant.

3.3. Results and discussion

Surface characterization

The physical analysis of the surfaces of the four experimental groups was carried out through FE-SEM, FIB, and AFM analysis (**Fig. 3.1**). There was a significant difference in the shape of the Co-Cr surface before and after the TIPS treatment. In the case of the Flat Co-Cr, control group, generally exhibited the smooth surface with few grinding marks generated during the polishing process. The Ta coated Co-Cr also showed a flat surface structure in line with control group. On the other hand, in the Nano-spike and Nano-ripple Co-Cr to which the TIPS was applied, the surfaces of Co-Cr were modified from smooth to nano-roughened surface. It was confirmed that the creation of these various nanostructures is directly controlled by the TIPS processing time (TIPS 5 min; Nano-spike Co-Cr, TIPS 30 min Nano-ripple Co-Cr). The Nano-spike Co-Cr had nano-scale protrusion parts, and the diameter of each pattern was about 100 nm. These nanostructures were not connected to each other and formed an independent pattern. On the other hand, in the nano-ripple Co-Cr, the patterns were connected to each other, and the length of the pattern was about 8 times longer than Nano-spike Co-Cr. For the cross-sectional images **Fig. 3.1B**, both Flat and Ta coated Co-Cr showed a flat surface without roughness, and the thickness of the Ta coating layer of Ta coated Co-Cr was about 100 nm. The depth of the formed nanostructures showed similar depths of about 500 nm in

both the Nano-spike and the Nano-ripple Co-Cr. The nano-scale struts were not connected to each other and existed independently in Nano-spike Co-Cr, whereas Nano-ripple Co-Cr has connected nano-struts corresponding to FE-SEM images. The average surface roughness of Flat and Ta coated Co-Cr showing a smooth surface was 3.3 ± 1.1 nm and 3.3 ± 0.1 nm, respectively. On the other hand, two nanostructured groups showed about 20 times higher average surface roughness than that of Flat and Ta coated Co-Cr (70.7 ± 7.7 , 72.2 ± 9.4 nm for Nano-spike and Nano-ripple Co-Cr, respectively) presented in **Fig. 3.1C**. In conclusion, it was confirmed that the Nano-spike Co-Cr inspired by dragonfly wing had a high structural similarity to that of a dragonfly wings as illustrated in **Table 2.1**. Especially, the aspect ratio of nanostructures, which is an important factor for mechano-antibacterial properties, has comparable value to the nanostructures of dragonfly wings. It was clearly confirmed that the TIPS treatment affects surface topography of Co-Cr throughout FE-SEM, FIB, and AFM surface observation.

Surface chemistry and hydrophilicity

STEM and EDS images show the physical and chemical changes in the Co-Cr surface since the TIPS process (**Fig. 3.2**). After TIPS treatment, it was confirmed that Ta atoms, which appear to be bright colored parts of the Co-Cr surface, were contained in the Co-Cr matrix, and the structure of Co-Cr was

changed into a deep and sharp needle morphology by Ta atom etching. The depth of Ta element contained in the Co-Cr substrate was present at an average of about 300 nm estimated by the EDS mapping image. The Ta atoms are present at the top of the nano-spike structure and exists without clear boundaries with Co-Cr. The content of Ta atoms incorporated into the Co-Cr matrix was the highest at about 30% in the upper part (p1), and the Ta content gradually decreased toward the substrate, showing almost 0% content in p3.

To evaluate the contact angle, which is one of the main factors affecting the bio-affinity of biomaterials, contact angle analysis was performed using the sessile drop method (**Fig. 3.3**). The contact angle of the Flat, Ta coated Co-Cr were $98 \pm 3^\circ$ and $37 \pm 1^\circ$, respectively. Ta coated Co-Cr showed half lower than that of the control group. Both the Nano-spike and Nano-ripple Co-Cr presented similar values as the Ta coated Co-Cr. The hydrophilic Ta component enhanced hydrophilicity of Co-Cr surface regardless of surface topography.

Although Co-Cr is a promising biomaterial due to its excellent strength, its use has been limited by low biocompatibility and antibacterial property. The low antibacterial property of Co-Cr bio-implants induces unexpected failure of implants caused by bacterial infection such as peri-implantitis and osteomyelitis, requiring re-surgery for implant placement eventually. In this study, we applied a novel strategy, TIPS, to Co-Cr implant

materials to mimics the structure of dragonfly wings with antibacterial property. The TIPS treated Co-Cr surface has nano-level spike structures exhibiting a mechanical antibacterial effect that physically ruptures bacteria cell walls. Besides, the nanostructures exhibit an excellent interaction with osteoblast cells because they are similar in size to the components of extracellular matrix.

TIPS technology was introduced using Ta as an etching source material to mimic the structure of dragonfly wings. The TIPS technology uses a high negative voltage applied to the substrate to accelerate the Ta cations emitted from the target. Accelerated Ta cations collide and deliver high impact energy to the substrate with creating unique nanostructures on the Co-Cr as described in **Fig. 3.1**. The variable that controls the topography of nanostructures is the TIPS process time. The Nano-spike Co-Cr with a process time of 5 min showed a nanostructure similar to the dragonfly wings with a high aspect ratio and independent nano-struts, whereas it turned into connected as the process time increased to 30 min. The nanostructures were connected to each other with forming a ripple pattern to minimize surface energy from the perspective thermodynamics [77]. As shown in the TEM images, Ta atoms selectively existed due to the difference in the local surface erosion rate leading to the creation of nanostructure. Nano-spike Co-Cr showed excellent hydrophilicity due to the presence of Ta elements and nanostructure which are the cause of enhanced hydrophilicity [24, 26, 78].

Evaluation of antibacterial properties

Antibacterial tests were performed by gram-negative (*E. coli*) and gram-positive (*S. aureus*), which are the major causes of implant infection (**Fig. 3.4**). Live and dead bacteria were visualized using fluorescent CLSM and FE-SEM observation depicted in **Fig. 3.4A**. For the Flat Co-Cr, it was confirmed that both *E. coli* and *S. aureus* survived and colonized throughout the entire Co-Cr surface in CLSM images. FE-SEM was performed to closely observe the adhered shape of the bacteria on the nanostructured surface. The *E. coli* and *S. aureus* maintained its rod and spherical shape without any sign of physical rupture in Flat Co-Cr, respectively. From the CLSM and FE-SEM images of Ta-coated Co-Cr, the bacteria that had grown over the entire surface were shown and no damage on bacteria membrane occurred. Almost all the bacteria were dead shown in red fluorescent on the Nano-spike Co-Cr surface, which has a biomimetic nano-surface. Especially, both types of bacterial membranes were physically ruptured with the intracellular cytoplasm leakage on Nano-spike Co-Cr. On the other hand, in the Nano-ripple Co-Cr having a connected nano-pattern structure presented similar results to those of the two smooth groups (Flat and Ta coated Co-Cr groups). It was proved that the nano-ripple surface did not impart mechano-antibacterial effect to Co-Cr. The percentage of killed bacteria was estimated using CLSM fluorescent images (**Fig. 3.4C**). According to a quantitative data, all the groups except for Nano-spike Co-Cr

showed killing efficiency against gram-negative and gram-positive bacteria of less than about 5%. There was no statistically significant difference among the three groups. On the other hand, the Nano-spike Co-Cr, which imitated the wings of dragonfly, showed an excellent antibacterial ability of about 70% (*E. coli*) and 50% (*S. aureus*).

The evaluation of antibacterial property was quantified using the bacterial colony count test as shown in **Fig. 3.4B**. The value of colony count of *E. coli* was 10.87, 9.28, 3.53, and 9.09×10^4 CFU for Flat, Ta coated, Nano-spike, and Nano-ripple Co-Cr, respectively. The number of *E. coli* colony showed a remarkable decrease in Nano-spike Co-Cr compared to the other groups by about 60% or more. As a result of the colony test using *S. aureus*, the colony count of Flat, Ta coated, Nano-spike, and Nano-ripple Co-Cr were 13.026, 12.666, 6.36, and 11.97×10^4 CFU, respectively. The Ta coated and Nano-ripple Co-Cr are not statistically different compared to Flat Co-Cr. On the other hand, it was found that the number of bacteria on Nano-spike Co-Cr decreased by about 50% compared with Flat Co-Cr. In the bacterial colony count tests with two types of bacteria, Ta coated and Nano-ripple Co-Cr did not show any statistical significance against Flat Co-Cr. On the other hand, only Nano-spike Co-Cr showed a dramatic decrease in bacterial colony formation compared to Flat Co-Cr. Bacterial adhesion and colony count tests were performed to evaluate the antibacterial activity of experimental groups. In a

bacterial adhesion test, gram-negative and gram-positive bacteria attached to the Nano-spike Co-Cr surface showed ruptured bacteria and release of cytoplasm which are clear signs for bacteria cell death. Bacterial colony count also confirmed that the lowest number of bacteria survived on the Nano-spike Co-Cr among the groups. As a result of various antibacterial tests, it was concluded that Nano-spike Co-Cr with the bio-inspired nanostructures through the TIPS process, has an excellent antibacterial activity.

In terms of antibacterial effect, the topographical characteristics of nanostructure are important factors to regulate growth in bacteria. The essential matters required for antibacterial property are high aspect ratios and independent nanostructure [75, 79]. The nano-spike structure is an ideal structure that physically stimulates the bacteria cell walls and finally induces rupture. Nano-spike Co-Cr showed excellent antibacterial properties against both gram-positive and gram-negative bacteria. Bacteria adhering to the Nano-spike Co-Cr surface are subject to mechanical tension of bacteria cell walls resulting in the membrane rupture and cytoplasm leakage [80-82]. The bacteria killing efficiency was reduced by about 20% in *S. aureus* compared to *E. coli*, due to structural difference of bacteria. The thickness of bacteria cell walls of *S. aureus* is about 20-100 nm, which is thicker than *E. coli* (≈ 5 nm) [83]. Hence, two types of bacteria have different resistance to external physical stimuli, and thus *S. aureus* has greater resistance to external stimuli than *E. coli*. Although

the surface was modified at the nano-level, Nano-ripple Co-Cr did not reveal antibacterial activity compared with the control group. Nano-ripple structures was not able to rupture the bacterial cell walls because they have a large surface area supporting bacteria physically [84]. Bacterial colony count test was performed to check the ability to suppress bacterial growth on the Flat, Ta coated, Nano-spike, and Nano-ripple Co-Cr. All the experimental groups showed similar trend in bacterial growth except for Nano-spike Co-Cr which quantitatively matches well with previous bacteria adhesion test. As a result, nano-spike Co-Cr exhibited excellent resistance to both bacteria attachment and growth.

Osteoblast cells attachment, proliferation, and differentiation tests

Cell adhesion, proliferation, and differentiation were evaluated to confirm the cell affinity of osteoblasts on each surface **Fig. 3.5**. The osteoblast adhesion was observed after culturing the osteoblast cells for 3 hr. The cell nuclei and cytoplasm were displayed in blue and red, respectively (**Fig. 3.5A**). For the CLSM low-magnification images, Flat Co-Cr showed that the attached osteoblast cells were close to a spherical shape with small spreading area. Ta coated Co-Cr exhibited an extensive cell spreading area than that of Flat Co-Cr resulting from incorporation of biocompatible Ta element. On the other hand, Nano-spike and Nano-ripple Co-Cr containing Ta elements, osteoblast cells not

only strongly attached to the nanostructured surface, but also showed highly activated filopodia which are positive signals leading to excellent biocompatibility. The surface coverage rate of osteoblasts was quantified from CLSM cell attachment images (**Fig. 3.5B**). The average surface coverage rate of osteoblast cells in Flat, Ta coated, Nano-spike, and Nano-ripple Co-Cr are 13, 32, 48, and 42%, respectively. Cytocompatibility on osteoblast cells was clearly improved in all the experimental groups containing the biocompatible Ta atom whether the form of coated or incorporated on the surface.

Cell proliferation and differentiation assay were performed using MTS and ACP activity assay (**Figs. 3.5C-D**). Cell viability was improved with increasing culture time without any signals related to toxicity. However, the degree of an increase in cell viability was significantly different for each group. Flat Co-Cr has the lowest value of cell viability throughout every time interval. After Ta coating on Co-Cr surface, the average cell viability was improved. On the other hand, the Nano-spike and Nano-ripple Co-Cr showed remarkable enhancement of cell proliferation compared to the Flat Co-Cr after 6 days of culture with the percentage of 132 and 140%, respectively. From the perspective of ALP activity, Nano-spike and Nano-ripple Co-Cr showed ALP activity values 3.7 and 3.4 times higher than Flat Co-Cr, and Ta coated Co-Cr had comparable ALP activity to Flat Co-Cr. *In vitro* cytocompatibility tests were conducted using osteoblast cells to confirm its applicability as a medical

implant. The cell adhesion, proliferation, and differentiation results indicate high potential of bio-inspired Nano-spike Co-Cr as bone implants. The biocompatibility was demonstrated through *in vitro* osteoblast cells attachment, proliferation, and differentiation assay and co-culturing of osteoblast cells and bacteria on Flat, Ta coated, Nano-spike, and Nano-ripple Co-Cr. Ta coated, Nano-spike, and Nano-ripple Co-Cr did not induce any cytotoxicity in the tests after coating or incorporating Ta into Co-Cr matrix. An increase in cell attachment, proliferation rate, and ALP activity was observed all the groups compared to control group. Nano-structured groups possess strong cellular response resulting from its nano-scale structures regulating integrin-dependent cell adhesion signaling pathways [85]. It also stimulates cells having an intimate contact with nano-roughened surface to induce focal adhesion, which indicates a strong interaction between cell and implants. Nanostructured Co-Cr with enhanced hydrophilicity leading to an excellent affinity with blood, and prevention of immune reactions such as platelet attachment and protein denaturation [25].

Osteoblast cells/Bacteria Co-culturing

Bacteria and osteoblast cells co-culturing test was performed to mimic physiological condition in human body. After culturing of osteoblast cells with *E. coli* and *S. aureus* on four groups, the cell viability of osteoblast was

investigated using live/dead CLSM observation (**Fig. 3.6A**). After co-culturing of *E. coli* and osteoblast cells, Flat Co-Cr only showed a small amount of viable osteoblast cells. In particular, it was confirmed that a large number of osteoblast cells was killed with forming a spherical shape marked by red. Bacterial colonization is a predominant reaction inhibiting the space where osteoblast cells would attach as shown in inset FE-SEM image. Ta coated Co-Cr showed similar results to Flat Co-Cr resulting from the lack of antibacterial property. On the other hand, Nano-spike Co-Cr exhibited the surface covered by viable osteoblast cells with highly activated filopodia, and bacteria was clearly ruptured depicted in inset FE-SEM image. The Nano-ripple Co-Cr indicated a relatively large number of surviving osteoblast cells than Flat and Ta coated Co-Cr due to its nanostructure, however, a predominant reaction on the surface was colonization of bacteria. The results of the co-culturing test using *S. aureus* showed similar trend. For the Flat, Ta coated, and nano-ripple Co-Cr, *S. aureus* were present on the surfaces due to their low antibacterial activity. Most of the osteoblast cells was dead because biological environment was too harsh for osteoblast cells to grow. On the other hand, Nano-spike Co-Cr was covered by strongly attached osteoblast cells, however, *S. aureus* was ruptured by antibacterial nanostructures inspired by dragonfly wings. **Fig. 3.6B** showed the surface coverage rate of the surviving osteoblast cells quantified from CLSM images. Flat, Ta coated Co-Cr showed low osteoblast viability due to the bacterial infection. Notably, the Nano-spike Co-Cr provided the favorable

environment for the growth in osteoblast cells resulting from antibacterial effect. From the co-culturing test, an average surface coverage rate of osteoblast cells against *E. coli*, and *S. aureus* was 33%, 29.3%, respectively, which are the highest value among all the groups. These results are 30 times higher than that of Flat Co-Cr. The Nano-ripple Co-Cr also showed a significant increase in the viability of osteoblast cells compared to the control group due to the nanostructure providing a favorable environment for cell growth. It was concluded that the bio-inspired Nano-spike Co-Cr surface has excellent antibacterial properties as well as excellent cytocompatibility simultaneously. To imitate the physiological environment in which bone cells and bacteria coexist, we evaluated the viability of osteoblast cells using co-culturing of osteoblasts and bacteria as illustrated in **Fig. 3.6**. Bacteria induce an inflammatory reaction in tissues and damage mammalian cells such as osteoblast cells [86, 87]. Flat, Ta coated Co-Cr shows fluorescence images in which almost all osteoblasts died by bacterial infection. On the other hand, Nano-spike Co-Cr indicated growth in osteoblast cells all over the surface under the competitive environment with bacteria which means a predominant reaction was the growth and proliferation of osteoblast cells. Although Nano-ripple Co-Cr also exhibited slight increase in osteoblast cells coverage rate than Flat, Ta coated Co-Cr due to the presence of nanostructure, However, the predominant reaction on the surface was the colonization and proliferation of bacteria. The experimental results showed similar trends in both osteoblast cells

culturing test with *E. coli* and *S. aureus*. The average surface occupancy of the viable bone cells in all groups was lower when osteoblast cells were co-cultured with *S. aureus* than with *E. coli* corresponding results **Figs. 3.4C-D**. In co-culture system, the Nano-spike Co-Cr presented a multi-functional surface that was difficult for bacteria to survive and good for osteoblasts.

3.4. Conclusion

This is the first study to impart antibacterial properties to the surface of metallic bio-implants using TIPS technique, which is a novel method to functionalize the surface of biomaterials. After applying the TIPS to Co-Cr implant, the surface was modified to a nano-spike surface with a high structural similarity to the dragonfly wings. Biomimetic Nano-spike Co-Cr showed excellent mechano-bactericidal effects on both gram-negative and gram-positive bacteria in bacteria attachment and colony formation tests. The nano-structured Co-Cr surfaces exhibited enhanced affinity on osteoblast cells by inducing a focal adhesion leading to a strong interaction between osteoblast cells and bio-implants. Nano-spike Co-Cr showed a multifunctional surface that suppressed the attachment and growth of bacteria and promoted the attachment and proliferation of osteoblasts in co-culturing test of osteoblast cells and bacteria. This multifunctional bio-implants not only induces reduced inflammatory response, but also an accelerated bone regeneration when applied to orthopedic implant materials.

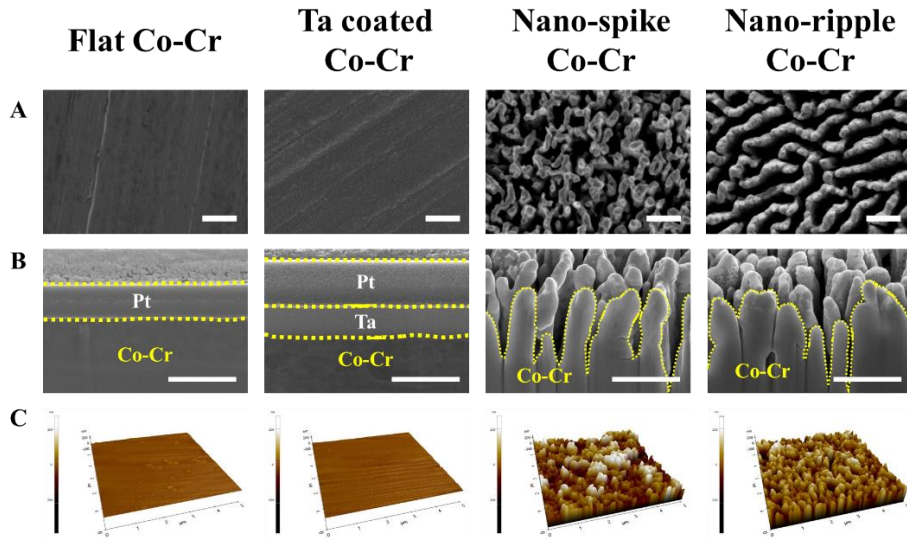


Figure 3.1. Representative surface morphologies of Flat, Ta coated, Nano-spike, and Nano-ripple: (a) field-emission scanning electron microscopy (FE-SEM), (b) the cross-sectional focused ion beam (FIB)/FE-SEM, and (c) Three-dimensional (3D) atomic force microscopy images. (Scale bar = 500 nm)

	Height (nm)	Distance (nm)	Diameter (nm)	Aspect ratio
Dragonfly wing	~ 330	~ 140	~ 60	~ 6
Nano-spike Co-Cr	~ 510	~ 210	~ 100	~ 5
Nano-ripple Co-Cr	~ 530	~ 270	~ 800	~ 1

Table 2.1. Average height, center to center distance, diameter and aspect ratio of nanospike for the comparison between dragonfly wing and Nano-spike Co-Cr.

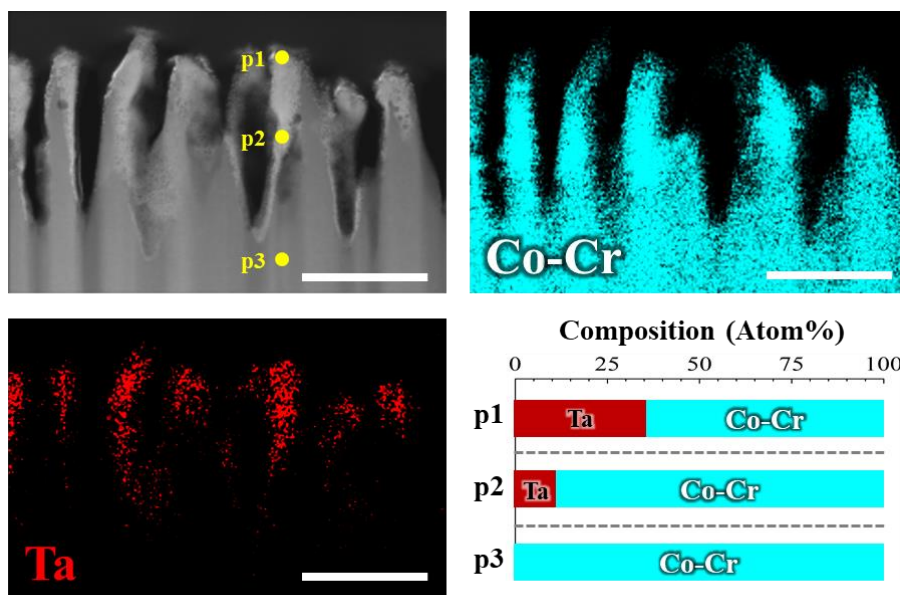


Figure 3.2. Cross-sectional scanning transmission electron microscopy image of Nano-spike Co-Cr with energy-dispersive X-ray spectroscopy mapping (Co-Cr and Ta elements), and chemical compositions at three regions in TEM image (p1: top, p2: middle, and p3: bottom). (Scale bar = 500 nm)

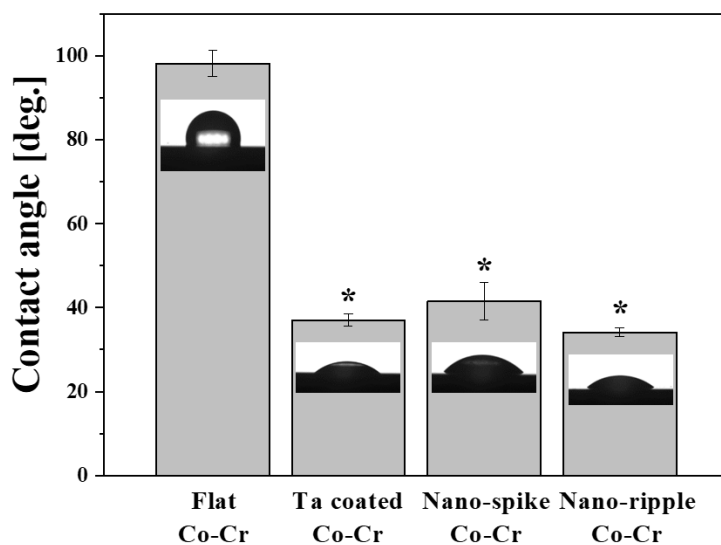


Figure 3.3. Water contact angles of Flat, Ta coated, Nano-spike, and Nano-ripple Co-Cr. Inset images denotes optical images of water droplets on each surface. (vs. Flat Co-Cr: $*p < 0.05$)

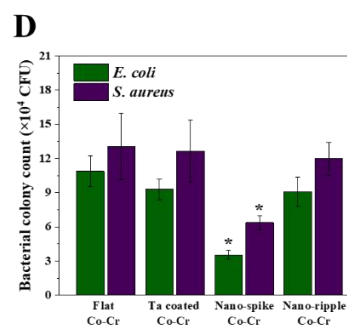
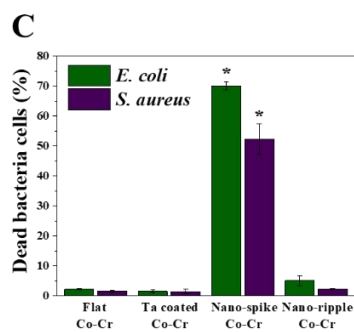
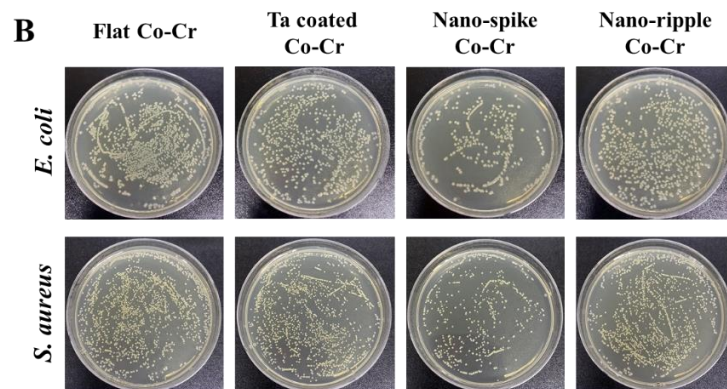
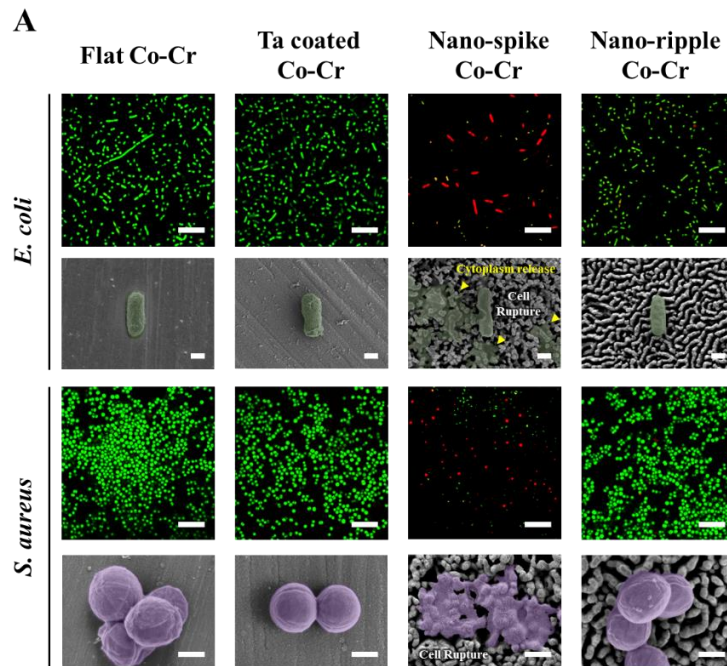


Figure 3.4. (A) Fluorescent images and FE-SEM images of *E. coli* and *S. aureus* cultured on Flat, Ta coated, Nano-spike, and Nano-ripple Co-Cr surfaces. The green and red fluorescence represent live and dead bacteria, respectively. The scale bar in the fluorescent CLSM and FE-SEM images are 10 μm and 500 nm, respectively. (B) Optical images of bacterial colony formation on agar plate after 12 hr of *E. coli* and *S. aureus* incubation. (C) The percentage of dead bacteria on Flat, Ta coated, Nano-spike, and Nano-ripple Co-Cr calculated by CLSM images. (D) Bacteria colony count of *E. coli* and *S. aureus* estimated using optical images of bacteria colony formation. White scale bars indicate 10 μm and 500 nm for fluorescent CLSM and FE-SEM images, respectively. (vs. Flat Co-Cr: $*p < 0.05$)

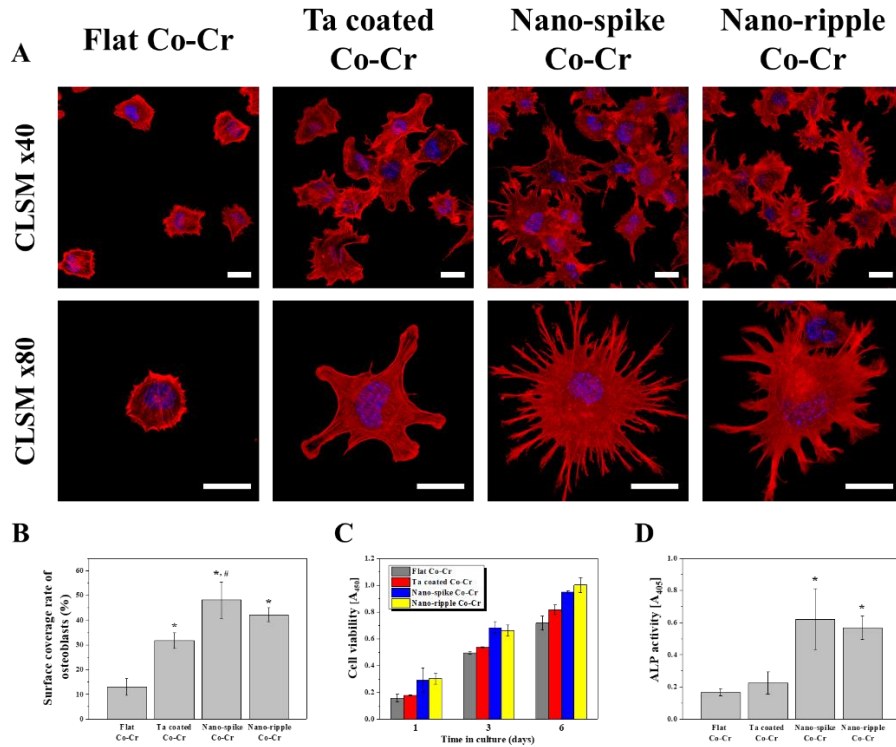


Figure 3.5. (A) Low (upper) and high (lower) magnification CLSM images of osteoblast cells adhered on the surfaces of Flat, Ta coated, Nano-spike, and Nano-ripple Co-Cr. (B) The surface coverage rate of osteoblast cells on Flat, Ta coated, Nano-spike, and Nano-ripple Co-Cr quantified from CLSM images. (C) Cell proliferation, and (D) differentiation (ALP activity) of osteoblast cells on each sample after 1, 3, and 6 days and 14 days, respectively. (vs. Flat Co-Cr: * $p < 0.05$, and vs. Ta coated Co-Cr: [#] $p < 0.05$)

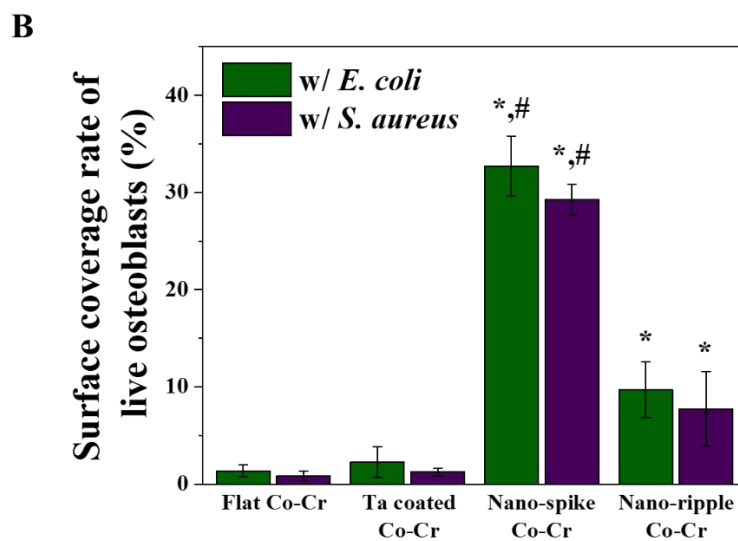
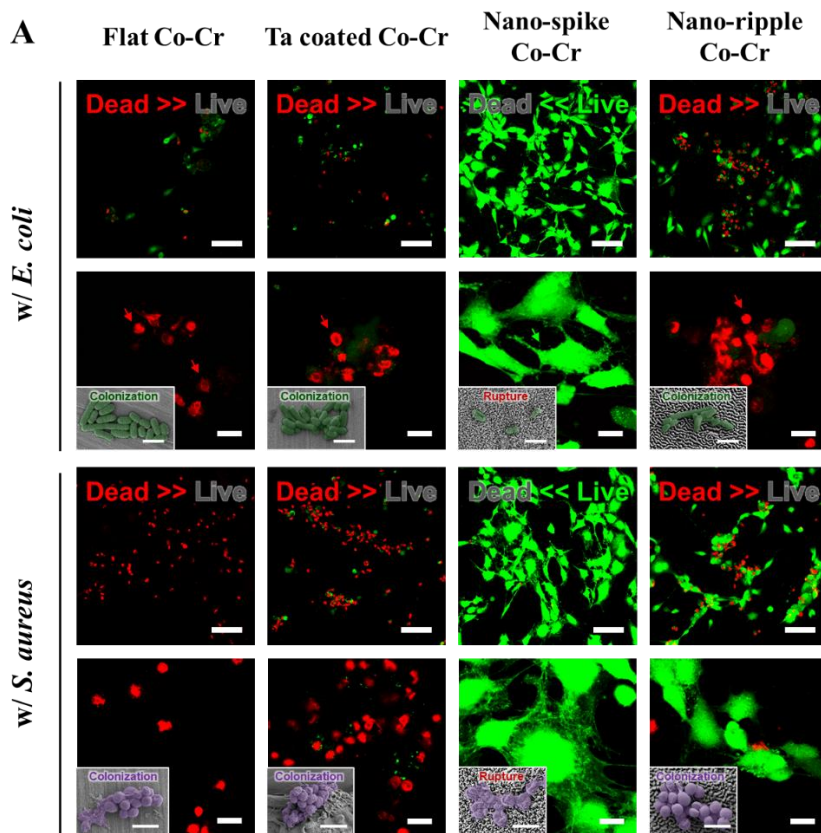


Figure 3.6. Low (upper) and high (lower) magnification CLSM images of osteoblast cells on the surfaces of Flat, Ta coated, Nano-spike, and Nano-ripple Co-Cr co-cultured with (A) *E. coli* and (B) *S. aureus*, respectively. The insets at the left corner of high magnification images are FE-SEM images of *E. coli* and *S. aureus* on each surface. (C) The surface coverage rate of live osteoblast cells after 24 hr of co-culturing with *E. coli* and *S. aureus*. (vs. Flat Co-Cr: * $p < 0.05$, and vs. Nano-ripple: # $p < 0.05$)

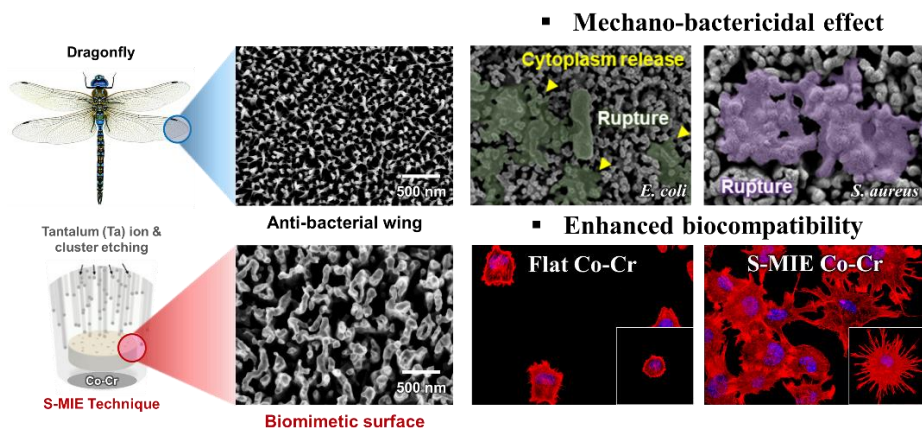


Figure 3.7. Schematic diagram of multi-functional Co-Cr bio-implants via Target-ion Induced Plasma Sputtering (TIPS).

Chapter 4.

Conclusion

4. Conclusion

The purpose of this thesis is to overcome existing limitations of metallic bio-implant materials and to impart various bio-functions to metallic bio-implants by utilizing the TIPS process. In conclusion, the TIPS process was applied to the surface of metallic bio-implants to achieve multi-functional surfaces. Based on the results of this study, it is concluded that the TIPS technology not only can be applied to various metal materials and but also is a promising technique that can offer specific functions depending on where metals are used for.

References

- [1] M.S. Sabatine, R.P. Giugliano, A.C. Keech, N. Honarpour, S.D. Wiviott, S.A. Murphy, J.F. Kuder, H. Wang, T. Liu, S.M. Wasserman, P.S. Sever, T.R. Pedersen, Evolocumab and Clinical Outcomes in Patients with Cardiovascular Disease, *New England Journal of Medicine* 376(18) (2017) 1713-1722.
- [2] R. Rasouli, A. Barhoum, H. Uludag, A review of nanostructured surfaces and materials for dental implants: surface coating, patterning and functionalization for improved performance, *Biomaterials Science* 6(6) (2018) 1312-1338.
- [3] C. Li, C. Guo, V. Fitzpatrick, A. Ibrahim, M.J. Zwierstra, P. Hanna, A. Lechtig, A. Nazarian, S.J. Lin, D.L. Kaplan, Design of biodegradable, implantable devices towards clinical translation, *Nature Reviews Materials* 5(1) (2020) 61-81.
- [4] D. Guadarrama Bello, A. Fouillen, A. Badia, A. Nanci, A nanoporous titanium surface promotes the maturation of focal adhesions and formation of filopodia with distinctive nanoscale protrusions by osteogenic cells, *Acta Biomaterialia* 60 (2017) 339-349.
- [5] H. Hermawan, A. Purnama, D. Dube, J. Couet, D. Mantovani, Fe-Mn alloys for metallic biodegradable stents: degradation and cell viability studies, *Acta Biomater* 6(5) (2010) 1852-60.
- [6] T.-S. Jang, J.H. Lee, S. Kim, C. Park, J. Song, H.J. Jae, H.-E. Kim, J.W. Chung, H.-D. Jung, Ta ion implanted nanoridge-platform for enhanced vascular responses, *Biomaterials* 223 (2019) 119461.
- [7] G.-N. Li, S.-M. Zhu, J.-F. Nie, Y. Zheng, Z. Sun, Investigating the stress corrosion cracking of a biodegradable Zn-0.8 wt%Li alloy in simulated body fluid, *Bioactive Materials* 6(5) (2021) 1468-1478.
- [8] W. Lin, H. Zhang, W. Zhang, H. Qi, G. Zhang, J. Qian, X. Li, L. Qin, H. Li, X. Wang, H. Qiu, X. Shi, W. Zheng, D. Zhang, R. Gao, J. Ding, In vivo degradation and endothelialization of an iron bioresorbable scaffold, *Bioactive Materials* 6(4) (2021) 1028-1039.
- [9] X. Tong, W. Cai, J. Lin, K. Wang, L. Jin, Z. Shi, D. Zhang, J. Lin, Y. Li, M. Dargusch, C. Wen, Biodegradable Zn-3Mg-0.7Mg₂Si composite fabricated by high-pressure solidification for bone implant applications, *Acta Biomaterialia*

123 (2021) 407-417.

[10] W. Pachla, S. Przybysz, A. Jarzębska, M. Bieda, K. Sztwiertnia, M. Kulczyk, J. Skiba, Structural and mechanical aspects of hypoeutectic Zn–Mg binary alloys for biodegradable vascular stent applications, *Bioactive Materials* 6(1) (2021) 26-44.

[11] C. Zhou, H.-F. Li, Y.-X. Yin, Z.-Z. Shi, T. Li, X.-Y. Feng, J.-W. Zhang, C.-X. Song, X.-S. Cui, K.-L. Xu, Y.-W. Zhao, W.-B. Hou, S.-T. Lu, G. Liu, M.-Q. Li, J.-y. Ma, E. Toft, A.A. Volinsky, M. Wan, X.-j. Yao, C.-b. Wang, K. Yao, S.-k. Xu, H. Lu, S.-F. Chang, J.-B. Ge, L.-N. Wang, H.-J. Zhang, Long-term in vivo study of biodegradable Zn-Cu stent: A 2-year implantation evaluation in porcine coronary artery, *Acta Biomaterialia* 97 (2019) 657-670.

[12] S.W. Lee, K.S. Phillips, H. Gu, M. Kazemzadeh-Narbat, D. Ren, How microbes read the map: Effects of implant topography on bacterial adhesion and biofilm formation, *Biomaterials* 268 (2021) 120595.

[13] H. Ishihama, K. Ishii, S. Nagai, H. Kakinuma, A. Sasaki, K. Yoshioka, T. Kuramoto, Y. Shiono, H. Funao, N. Isogai, T. Tsuji, Y. Okada, S. Koyasu, Y. Toyama, M. Nakamura, M. Aizawa, M. Matsumoto, An antibacterial coated polymer prevents biofilm formation and implant-associated infection, *Scientific Reports* 11(1) (2021) 3602.

[14] R. Liu, Y. Tang, L. Zeng, Y. Zhao, Z. Ma, Z. Sun, L. Xiang, L. Ren, K. Yang, In vitro and in vivo studies of anti-bacterial copper-bearing titanium alloy for dental application, *Dental Materials* 34(8) (2018) 1112-1126.

[15] E.A. Masters, R.P. Trombetta, K.L. de Mesy Bentley, B.F. Boyce, A.L. Gill, S.R. Gill, K. Nishitani, M. Ishikawa, Y. Morita, H. Ito, S.N. Bello-Irizarry, M. Ninomiya, J.D. Brodell, C.C. Lee, S.P. Hao, I. Oh, C. Xie, H.A. Awad, J.L. Daiss, J.R. Owen, S.L. Kates, E.M. Schwarz, G. Muthukrishnan, Evolving concepts in bone infection: redefining “biofilm”, “acute vs. chronic osteomyelitis”, “the immune proteome” and “local antibiotic therapy”, *Bone Research* 7(1) (2019) 20.

[16] H. Yang, X. Qu, W. Lin, C. Wang, D. Zhu, K. Dai, Y. Zheng, In vitro and in vivo studies on zinc-hydroxyapatite composites as novel biodegradable metal matrix composite for orthopedic applications, *Acta Biomaterialia* 71 (2018) 200-214.

[17] Y. Su, I. Cockerill, Y. Zheng, L. Tang, Y.-X. Qin, D. Zhu, Biofunctionalization of metallic implants by calcium phosphate coatings,

Bioactive Materials 4 (2019) 196-206.

[18] N. Kröger, A. Kopp, M. Staudt, M. Rusu, A. Schuh, E.A. Liehn, Hemocompatibility of plasma electrolytic oxidation (PEO) coated Mg-RE and Mg-Zn-Ca alloys for vascular scaffold applications, *Materials Science and Engineering: C* 92 (2018) 819-826.

[19] R.I.M. Asri, W.S.W. Harun, M. Samykano, N.A.C. Lah, S.A.C. Ghani, F. Tarlochan, M.R. Raza, Corrosion and surface modification on biocompatible metals: A review, *Materials Science and Engineering: C* 77 (2017) 1261-1274.

[20] C. Park, S. Kim, H.-E. Kim, T.-S. Jang, Mechanically stable tantalum coating on a nano-roughened NiTi stent for enhanced radiopacity and biocompatibility, *Surface and Coatings Technology* 305 (2016) 139-145.

[21] V. Ständert, K. Borcherdig, N. Bormann, G. Schmidmaier, I. Grunwald, B. Wildemann, Antibiotic-loaded amphora-shaped pores on a titanium implant surface enhance osteointegration and prevent infections, *Bioactive Materials* 6(8) (2021) 2331-2345.

[22] M. Riaz, V. Mutreja, S. Sareen, B. Ahmad, M. Faheem, N. Zahid, G. Jabbour, J. Park, Exceptional antibacterial and cytotoxic potency of monodisperse greener AgNPs prepared under optimized pH and temperature, *Scientific Reports* 11(1) (2021) 2866.

[23] S. Kim, C. Park, K.-H. Cheon, H.-D. Jung, J. Song, H.-E. Kim, T.-S. Jang, Antibacterial and bioactive properties of stabilized silver on titanium with a nanostructured surface for dental applications, *Applied Surface Science* 451 (2018) 232-240.

[24] C. Park, S. Park, J. Kim, A. Han, S. Ahn, S.-K. Min, H.J. Jae, J.W. Chung, J.-H. Lee, H.-D. Jung, H.-E. Kim, T.-S. Jang, Enhanced endothelial cell activity induced by incorporation of nano-thick tantalum layer in artificial vascular grafts, *Applied Surface Science* 508 (2020) 144801.

[25] C. Park, Y.-J. Seong, I.-G. Kang, E.-H. Song, H. Lee, J. Kim, H.-D. Jung, H.-E. Kim, T.-S. Jang, Enhanced Osseointegration Ability of Poly(lactic acid) via Tantalum Sputtering-Based Plasma Immersion Ion Implantation, *ACS Applied Materials & Interfaces* 11(11) (2019) 10492-10504.

[26] C. Park, S.-W. Lee, J. Kim, E.-H. Song, H.-D. Jung, J.-U. Park, H.-E. Kim, S. Kim, T.-S. Jang, Reduced fibrous capsule formation at nano-engineered silicone surfaces via tantalum ion implantation, *Biomaterials Science* 7(7)

(2019) 2907-2919.

[27] S.-W. Hwang, H. Tao, D.-H. Kim, H. Cheng, J.-K. Song, E. Rill, M.A. Brenckle, B. Panilaitis, S.M. Won, Y.-S. Kim, Y.M. Song, K.J. Yu, A. Ameen, R. Li, Y. Su, M. Yang, D.L. Kaplan, M.R. Zakin, M.J. Slepian, Y. Huang, F.G. Omenetto, J.A. Rogers, A Physically Transient Form of Silicon Electronics, *Science* 337(6102) (2012) 1640.

[28] S.-K. Kang, R.K.J. Murphy, S.-W. Hwang, S.M. Lee, D.V. Harburg, N.A. Krueger, J. Shin, P. Gamble, H. Cheng, S. Yu, Z. Liu, J.G. McCall, M. Stephen, H. Ying, J. Kim, G. Park, R.C. Webb, C.H. Lee, S. Chung, D.S. Wie, A.D. Gujar, B. Vemulapalli, A.H. Kim, K.-M. Lee, J. Cheng, Y. Huang, S.H. Lee, P.V. Braun, W.Z. Ray, J.A. Rogers, Bioresorbable silicon electronic sensors for the brain, *Nature* 530(7588) (2016) 71-76.

[29] M.-H. Kang, H. Lee, T.-S. Jang, Y.-J. Seong, H.-E. Kim, Y.-H. Koh, J. Song, H.-D. Jung, Biomimetic porous Mg with tunable mechanical properties and biodegradation rates for bone regeneration, *Acta Biomaterialia* 84 (2019) 453-467.

[30] Z. Lin, Y. Zhao, P.K. Chu, L. Wang, H. Pan, Y. Zheng, S. Wu, X. Liu, K.M.C. Cheung, T. Wong, K.W.K. Yeung, A functionalized TiO₂/Mg₂TiO₄ nano-layer on biodegradable magnesium implant enables superior bone-implant integration and bacterial disinfection, *Biomaterials* 219 (2019) 119372.

[31] H. Yang, B. Jia, Z. Zhang, X. Qu, G. Li, W. Lin, D. Zhu, K. Dai, Y. Zheng, Alloying design of biodegradable zinc as promising bone implants for load-bearing applications, *Nature Communications* 11(1) (2020) 401.

[32] Y. Qi, H. Qi, Y. He, W. Lin, P. Li, L. Qin, Y. Hu, L. Chen, Q. Liu, H. Sun, Q. Liu, G. Zhang, S. Cui, J. Hu, L. Yu, D. Zhang, J. Ding, Strategy of Metal–Polymer Composite Stent To Accelerate Biodegradation of Iron-Based Biomaterials, *ACS Applied Materials & Interfaces* 10(1) (2018) 182-192.

[33] D. Zhu, Y. Su, M.L. Young, J. Ma, Y. Zheng, L. Tang, Biological Responses and Mechanisms of Human Bone Marrow Mesenchymal Stem Cells to Zn and Mg Biomaterials, *ACS Applied Materials & Interfaces* 9(33) (2017) 27453-27461.

[34] Y.F. Zheng, X.N. Gu, F. Witte, Biodegradable metals, *Materials Science and Engineering: R: Reports* 77 (2014) 1-34.

[35] H. Wu, C. Zhang, T. Lou, B. Chen, R. Yi, W. Wang, R. Zhang, M. Zuo, H.

Xu, P. Han, S. Zhang, J. Ni, X. Zhang, Crevice corrosion – A newly observed mechanism of degradation in biomedical magnesium, *Acta Biomaterialia* 98 (2019) 152-159.

[36] P.K. Bowen, E.R. Shearier, S. Zhao, R.J. Guillory II, F. Zhao, J. Goldman, J.W. Drelich, Biodegradable Metals for Cardiovascular Stents: from Clinical Concerns to Recent Zn-Alloys, *Advanced Healthcare Materials* 5(10) (2016) 1121-1140.

[37] Y. Liu, Y. Zheng, X.-H. Chen, J.-A. Yang, H. Pan, D. Chen, L. Wang, J. Zhang, D. Zhu, S. Wu, K.W.K. Yeung, R.-C. Zeng, Y. Han, S. Guan, Fundamental Theory of Biodegradable Metals—Definition, Criteria, and Design, *Advanced Functional Materials* 29(18) (2019) 1805402.

[38] M. Peuster, P. Wohlsein, M. Brüggmann, M. Ehlerding, K. Seidler, C. Fink, H. Brauer, A. Fischer, G. Hausdorf, A novel approach to temporary stenting: degradable cardiovascular stents produced from corrodible metal—results 6–18 months after implantation into New Zealand white rabbits, 86(5) (2001) 563-569.

[39] T. Kraus, F. Moszner, S. Fischerauer, M. Fiedler, E. Martinelli, J. Eichler, F. Witte, E. Willbold, M. Schinhammer, M. Meischel, P.J. Uggowitzer, J.F. Löffler, A. Weinberg, Biodegradable Fe-based alloys for use in osteosynthesis: Outcome of an in vivo study after 52weeks, *Acta Biomaterialia* 10(7) (2014) 3346-3353.

[40] Y. Qi, X. Li, Y. He, D. Zhang, J. Ding, Mechanism of Acceleration of Iron Corrosion by a Polylactide Coating, *ACS Applied Materials & Interfaces* 11(1) (2019) 202-218.

[41] W. Lin, L. Qin, H. Qi, D. Zhang, G. Zhang, R. Gao, H. Qiu, Y. Xia, P. Cao, X. Wang, W. Zheng, Long-term in vivo corrosion behavior, biocompatibility and bioresorption mechanism of a bioresorbable nitrided iron scaffold, *Acta Biomaterialia* 54 (2017) 454-468.

[42] S.-K. Kang, S.-W. Hwang, S. Yu, J.-H. Seo, E.A. Corbin, J. Shin, D.S. Wie, R. Bashir, Z. Ma, J.A. Rogers, Biodegradable Thin Metal Foils and Spin-On Glass Materials for Transient Electronics, *Advanced Functional Materials* 25(12) (2015) 1789-1797.

[43] L. Yin, H. Cheng, S. Mao, R. Haasch, Y. Liu, X. Xie, S.-W. Hwang, H. Jain, S.-K. Kang, Y. Su, R. Li, Y. Huang, J.A. Rogers, Dissolvable Metals for Transient Electronics, *Advanced Functional Materials* 24(5) (2014) 645-658.

- [44] Q. Chen, G.A. Thouas, Metallic implant biomaterials, *Materials Science and Engineering: R: Reports* 87 (2015) 1-57.
- [45] R.J. Guillory, P.K. Bowen, S.P. Hopkins, E.R. Shearier, E.J. Earley, A.A. Gillette, E. Aghion, M. Bocks, J.W. Drelich, J. Goldman, Corrosion Characteristics Dictate the Long-Term Inflammatory Profile of Degradable Zinc Arterial Implants, *ACS Biomaterials Science & Engineering* 2(12) (2016) 2355-2364.
- [46] J. Zhou, Y. Yang, M. Alonso Frank, R. Detsch, A.R. Boccaccini, S. Virtanen, Accelerated Degradation Behavior and Cytocompatibility of Pure Iron Treated with Sandblasting, *ACS Applied Materials & Interfaces* 8(40) (2016) 26482-26492.
- [47] E. Ngandu Mpoyi, M. Cantini, P.M. Reynolds, N. Gadegaard, M.J. Dalby, M. Salmerón-Sánchez, Protein Adsorption as a Key Mediator in the Nanotopographical Control of Cell Behavior, *ACS Nano* 10(7) (2016) 6638-6647.
- [48] J.H. Kim, H.W. Kim, K.J. Cha, J. Han, Y.J. Jang, D.S. Kim, J.-H. Kim, Nanotopography Promotes Pancreatic Differentiation of Human Embryonic Stem Cells and Induced Pluripotent Stem Cells, *ACS Nano* 10(3) (2016) 3342-3355.
- [49] T.-S. Jang, S. Kim, H.-D. Jung, J.-W. Chung, H.-E. Kim, Y.-H. Koh, J. Song, Large-scale nanopatterning of metal surfaces by target-ion induced plasma sputtering (TIPS), *RSC Advances* 6(28) (2016) 23702-23708.
- [50] T. Lu, J. Wen, S. Qian, H. Cao, C. Ning, X. Pan, X. Jiang, X. Liu, P.K. Chu, Enhanced osteointegration on tantalum-implanted polyetheretherketone surface with bone-like elastic modulus, *Biomaterials* 51 (2015) 173-183.
- [51] C. Yang, J. Li, C. Zhu, Q. Zhang, J. Yu, J. Wang, Q. Wang, J. Tang, H. Zhou, H. Shen, Advanced antibacterial activity of biocompatible tantalum nanofilm via enhanced local innate immunity, *Acta Biomaterialia* 89 (2019) 403-418.
- [52] B. Liu, Y.F. Zheng, Effects of alloying elements (Mn, Co, Al, W, Sn, B, C and S) on biodegradability and in vitro biocompatibility of pure iron, *Acta Biomaterialia* 7(3) (2011) 1407-1420.
- [53] A.F. Cipriano, J. Lin, A. Lin, A. Sallee, B. Le, M.C. Cortez Alcaraz, R.-G. Guan, G. Botimer, S. Inceoglu, H. Liu, Degradation of Bioresorbable Mg-4Zn-

1Sr Intramedullary Pins and Associated Biological Responses in Vitro and in Vivo, *ACS Applied Materials & Interfaces* 9(51) (2017) 44332-44355.

[54] F. Witte, J. Fischer, J. Nellesen, H.-A. Crostack, V. Kaese, A. Pisch, F. Beckmann, H. Windhagen, In vitro and in vivo corrosion measurements of magnesium alloys, *Biomaterials* 27(7) (2006) 1013-1018.

[55] S. Maeng, L. Axe, T.A. Tyson, L. Gladczuk, M. Sosnowski, Corrosion behaviour of magnetron sputtered α - and β -Ta coatings on AISI 4340 steel as a function of coating thickness, *Corrosion Science* 48(8) (2006) 2154-2171.

[56] W. Jin, G. Wang, Z. Lin, H. Feng, W. Li, X. Peng, A.M. Qasim, P.K. Chu, Corrosion resistance and cytocompatibility of tantalum-surface-functionalized biomedical ZK60 Mg alloy, *Corrosion Science* 114 (2017) 45-56.

[57] M.D. Anderson, B. Aitchison, D.C. Johnson, Corrosion Resistance of Atomic Layer Deposition-Generated Amorphous Thin Films, *ACS Applied Materials & Interfaces* 8(44) (2016) 30644-30648.

[58] M. Schinhammer, P. Steiger, F. Moszner, J.F. Löffler, P.J. Uggowitzer, Degradation performance of biodegradable FeMnC(Pd) alloys, *Materials Science and Engineering: C* 33(4) (2013) 1882-1893.

[59] S. Zhu, N. Huang, L. Xu, Y. Zhang, H. Liu, H. Sun, Y. Leng, Biocompatibility of pure iron: In vitro assessment of degradation kinetics and cytotoxicity on endothelial cells, *Materials Science and Engineering: C* 29(5) (2009) 1589-1592.

[60] J.C. Doloff, O. Veiseh, A.J. Vegas, H.H. Tam, S. Farah, M. Ma, J. Li, A. Bader, A. Chiu, A. Sadraei, S. Aresta-Dasilva, M. Griffin, S. Jhunjhunwala, M. Webber, S. Siebert, K. Tang, M. Chen, E. Langan, N. Dholokia, R. Thakrar, M. Qi, J. Oberholzer, D.L. Greiner, R. Langer, D.G. Anderson, Colony stimulating factor-1 receptor is a central component of the foreign body response to biomaterial implants in rodents and non-human primates, *Nature Materials* 16(6) (2017) 671-680.

[61] X. Wang, S. Xu, S. Zhou, W. Xu, M. Leary, P. Choong, M. Qian, M. Brandt, Y.M. Xie, Topological design and additive manufacturing of porous metals for bone scaffolds and orthopaedic implants: A review, *Biomaterials* 83 (2016) 127-141.

[62] Z. Wang, X. Wang, J. Pei, Y. Tian, J. Zhang, C. Jiang, J. Huang, Z. Pang, Y. Cao, X. Wang, S. An, X. Wang, H. Huang, G. Yuan, Z. Yan, Degradation and

osteogenic induction of a SrHPO₄-coated Mg–Nd–Zn–Zr alloy intramedullary nail in a rat femoral shaft fracture model, *Biomaterials* 247 (2020) 119962.

[63] C. Hu, D. Ashok, D.R. Nisbet, V. Gautam, Bioinspired surface modification of orthopedic implants for bone tissue engineering, *Biomaterials* 219 (2019) 119366.

[64] L.C. Zhang, L.Y. Chen, A Review on Biomedical Titanium Alloys: Recent Progress and Prospect, *Advanced Engineering Materials* 21(4) (2019).

[65] X.Y. Zhang, G. Fang, S. Leeftang, A.A. Zadpoor, J. Zhou, Topological design, permeability and mechanical behavior of additively manufactured functionally graded porous metallic biomaterials, *Acta Biomaterialia* 84 (2019) 437-452.

[66] T.C. Paim, D.P. Wermuth, I. Bertaco, C. Zanatelli, L.I.S. Naasani, M. Slaviero, D. Driemeier, L. Schaeffer, M.R. Wink, Evaluation of in vitro and in vivo biocompatibility of iron produced by powder metallurgy, *Materials Science and Engineering: C* 115 (2020) 111129.

[67] K. Chen, Y. Lu, H. Tang, Y. Gao, F. Zhao, X. Gu, Y. Fan, Effect of strain on degradation behaviors of WE43, Fe and Zn wires, *Acta Biomaterialia* 113 (2020) 627-645.

[68] E. Zhang, C. Liu, A new antibacterial Co–Cr–Mo–Cu alloy: Preparation, biocorrosion, mechanical and antibacterial property, *Materials Science and Engineering: C* 69 (2016) 134-143.

[69] T. Wei, Q. Yu, H. Chen, Responsive and Synergistic Antibacterial Coatings: Fighting against Bacteria in a Smart and Effective Way, *Advanced Healthcare Materials* 8(3) (2019) 1801381.

[70] Y. Zhang, P. Sun, L. Zhang, Z. Wang, F. Wang, K. Dong, Z. Liu, J. Ren, X. Qu, Silver-Infused Porphyrinic Metal–Organic Framework: Surface-Adaptive, On-Demand Nanoplatfrom for Synergistic Bacteria Killing and Wound Disinfection, *Advanced Functional Materials* 29(11) (2019) 1808594.

[71] D. Gil, A.E. Atici, R.L. Connolly, S. Hugard, S. Shuvaev, K.K. Wannomae, E. Oral, O.K. Muratoglu, Addressing prosthetic joint infections via gentamicin-eluting UHMWPE spacer, *The Bone & Joint Journal* 102-B(6_Supple_A) (2020) 151-157.

[72] A.-C. Burdușel, O. Gherasim, A.M. Grumezescu, L. Mogoantă, A. Ficai,

E. Andronesco, Biomedical Applications of Silver Nanoparticles: An Up-to-Date Overview, *Nanomaterials* 8(9) (2018) 681.

[73] J. Li, X. Liu, L. Tan, Z. Cui, X. Yang, Y. Liang, Z. Li, S. Zhu, Y. Zheng, K.W.K. Yeung, X. Wang, S. Wu, Zinc-doped Prussian blue enhances photothermal clearance of *Staphylococcus aureus* and promotes tissue repair in infected wounds, *Nature Communications* 10(1) (2019) 4490.

[74] R. Liang, Y. Xu, M. Zhao, G. Han, J. Li, W. Wu, M. Dong, J. Yang, Y. Liu, Properties of silver contained coatings on CoCr alloys prepared by vacuum plasma spraying, *Materials Science and Engineering: C* 106 (2020) 110156.

[75] E.P. Ivanova, J. Hasan, H.K. Webb, G. Gervinskas, S. Juodkazis, V.K. Truong, A.H. Wu, R.N. Lamb, V.A. Baulin, G.S. Watson, J.A. Watson, D.E. Mainwaring, R.J. Crawford, Bactericidal activity of black silicon, *Nat Commun* 4 (2013) 2838.

[76] C.D. Bandara, S. Singh, I.O. Afara, A. Wolff, T. Tesfamichael, K. Ostrikov, A. Oloyede, Bactericidal Effects of Natural Nanotopography of Dragonfly Wing on *Escherichia coli*, *ACS Appl Mater Interfaces* 9(8) (2017) 6746-6760.

[77] I. Yamada, J. Matsuo, N. Toyoda, T. Aoki, T. Seki, Progress and applications of cluster ion beam technology, *Current Opinion in Solid State and Materials Science* 19(1) (2015) 12-18.

[78] K.-H. Cheon, C. Park, M.-H. Kang, I.-G. Kang, M.-K. Lee, H. Lee, H.-E. Kim, H.-D. Jung, T.-S. Jang, Construction of tantalum/poly(ether imide) coatings on magnesium implants with both corrosion protection and osseointegration properties, *Bioactive Materials* 6(4) (2021) 1189-1200.

[79] E.P. Ivanova, S.H. Nguyen, Y. Guo, V.A. Baulin, H.K. Webb, V.K. Truong, J.V. Wandiyanto, C.J. Garvey, P.J. Mahon, D.E. Mainwaring, R.J. Crawford, Bactericidal activity of self-assembled palmitic and stearic fatty acid crystals on highly ordered pyrolytic graphite, *Acta Biomater* 59 (2017) 148-157.

[80] S. Pogodin, J. Hasan, V.A. Baulin, H.K. Webb, V.K. Truong, T.H. Phong Nguyen, V. Boshkovikj, C.J. Fluke, G.S. Watson, J.A. Watson, R.J. Crawford, E.P. Ivanova, Biophysical model of bacterial cell interactions with nanopatterned cicada wing surfaces, *Biophys J* 104(4) (2013) 835-40.

[81] Y. Tang, H. Sun, Z. Qin, S. Yin, L. Tian, Z. Liu, Bioinspired photocatalytic ZnO/Au nanopillar-modified surface for enhanced antibacterial and antiadhesive property, *Chemical Engineering Journal* 398 (2020) 125575.

- [82] Q. Gao, T. Feng, D. Huang, P. Liu, P. Lin, Y. Wu, Z. Ye, J. Ji, P. Li, W. Huang, Antibacterial and hydroxyapatite-forming coating for biomedical implants based on polypeptide-functionalized titania nanospikes, *Biomater Sci* 8(1) (2019) 278-289.
- [83] A. Tripathy, P. Sen, B. Su, W.H. Briscoe, Natural and bioinspired nanostructured bactericidal surfaces, *Adv Colloid Interface Sci* 248 (2017) 85-104.
- [84] F. Xue, J. Liu, L. Guo, L. Zhang, Q. Li, Theoretical study on the bactericidal nature of nanopatterned surfaces, *J Theor Biol* 385 (2015) 1-7.
- [85] B.-S. Moon, S. Kim, H.-E. Kim, T.-S. Jang, Hierarchical micro-nano structured Ti6Al4V surface topography via two-step etching process for enhanced hydrophilicity and osteoblastic responses, *Materials Science and Engineering: C* 73 (2017) 90-98.
- [86] V.T. Pham, V.K. Truong, A. Orlowska, S. Ghanaati, M. Barbeck, P. Booms, A.J. Fulcher, C.M. Bhadra, R. Buividas, V. Baulin, C.J. Kirkpatrick, P. Doran, D.E. Mainwaring, S. Juodkazis, R.J. Crawford, E.P. Ivanova, "Race for the Surface": Eukaryotic Cells Can Win, *ACS Appl Mater Interfaces* 8(34) (2016) 22025-31.
- [87] B. Mehrjou, S. Mo, D. Dehghan-Baniani, G. Wang, A.M. Qasim, P.K. Chu, Antibacterial and Cytocompatible Nanoengineered Silk-Based Materials for Orthopedic Implants and Tissue Engineering, *ACS Appl Mater Interfaces* 11(35) (2019) 31605-31614.

Abstract (Korean)

국문 초록

금속 생체 임플란트의 표면 기능화

서울대학교

재료공학부

이 민 규

우수한 생체적합성, 강도를 가지는 금속재료는 수십년에 걸쳐 의료분야에서 널리 사용되어온 재료이다. 혈관용 스텐트, 뼈 및 치아용 금속 임플란트 재료는 체내 손상된 조직을 효과적으로 지지하고 대체할 수 있다. 그러나 이식 후 불 균일한 부식 거동과 심한 염증 반응은 이의 사용을 제한하는 가장 큰 문제점이다. 따라서, 이러한 문제를 해결하기 위해 금속 생체 임플란트 표면에 다양한 생기능성을 부여하기위한 표면 처리 방법이 활발하게 연구되어왔다. 임플란트 표면에 금속 및 약물 코팅을 하는 방법은 금속 임플란트의 생기능성을 부여하기위한 가장 쉽고 편리한 방법이다. 이러한 성과에도 불구하고, 이 방법은 낮은 코팅 안정성으로 인한 코팅층 박

리가 발생하고 이로 인해 체내 부작용을 유발한다는 문제점을 지닌다.

본 연구에서, 기존 금속 박막 증착 방식인 스퍼터링 기술을 이용한 금속 생체 임플란트의 간단하고 효과적인 표면 처리 방법을 개발하였다. 스퍼터링 기반의 금속 이온 에칭 (TIPS)은 금속 타겟에서 방출되는 금속 양이온을 사용하여 기판 금속을 식각하는 기술이다. 타겟으로부터 방출된 금속 양이온은 기판 금속에 인가된 매우 높은 음의 전압에 의해 가속화 되어 기판 물질에 큰 충격을 가하며 충돌한다. 이러한 금속 이온에 의한 식각 과정에서 기판 표면에 나노수준의 독특한 구조가 형성되고 이로 인해 금속 생체 임플란트 표면은 다양한 생기능성을 띠게 된다. 이러한 공정은 기존 박막 코팅 스퍼터링 공정과 비교하여 타겟 금속 이온이 강력하게 기판 금속과 충돌하였으므로 주입된 타겟 이온과 금속 기판 물질 사이 우수한 기계적 안정성을 보인다. TIPS 공정은 금속 임플란트 표면에 형성한 독특한 나노구조로 인해 금속의 제어 가능한 부식 거동 및 우수한 항균특성과 같은 다양한 생기능을 제공한다. 본 연구에서 타겟 물질로 우수한 생체적합성을 가지는 금속 원자로 알려진 탄탈륨 (Ta)가 사용되었다. Ta는 큰 원자량을 가지고 있어 금속 임플란트 표면에 보다 큰 충격에너지를 가해 금속 임플란트 표면을 효과적으로 식각 할 수 있는 금속재료이다.

첫 번째 연구는 생분해성 임플란트 소재로의 응용을 위한 Ta과 Fe가 통합된 생분해성 재료에 관한 연구이다. 최근 철은 우수

한 기계적, 생물학적 특성으로 혈관, 정형외과용 기기 분야에서 각광받는 소재이다. 그러나 생리적 조건 하에서 Fe는 매우 느린 분해 속도와 불 균일한 부식거동을 보인다. 이러한 문제는 Fe가 의료용 임플란트 재료로 사용되었을 때 체내 심각한 부작용을 유발하는 심각한 한계점이다. 따라서 본 연구에서는 Fe 임플란트의 빠르고 균일한 부식거동을 실현하기 위해 Ta를 포함하는 나노구조화된 Fe를 개발하였다. TIPS 기술을 Fe 임플란트에 적용하여 전기화학적으로 높은 전위를 가지는 Ta를 그 표면에 도입하여 갈바닉 부식을 유도하였고, 더불어 생체적합성이 우수한 Ta를 포함시켜 생체적합성까지 동시에 향상시키는 다기능성 임플란트 재료를 개발하였다. TIPS 공정에서 스퍼터링 건에서 생성된 다수의 Ta 양이온이 높은 음 전압이 인가된 기관쪽으로 가속화되어 Fe 표면에 주입되었다. 결과적으로, Fe 임플란트 재료 표면에 Ta를 포함하는 독특한 나노구조를 형성시켰다. 나노 구조 표면의 상단에 상당한 양의 Ta (50 at %)가 포함되어 있었고 이로 인해, Fe 표면에서 갈바닉 부식이 유도되어 TIPS 공정이 적용되지 않은 Bare Fe 대비 가속화되고 균일한 부식이 관찰되었다. 또한 균일한 부식거동을 보이는 나노 Ta-Fe의 기계적 특성은 장기간의 시험관 내 부식 시험 (40 주) 후에도 거의 일정하게 유지되었다. 생체 적합성은 시험관 내 골아 세포 실험 및 토끼 동물실험 골수 내강 이식 모델을 사용하여 Bare Fe 및 나노 Ta-Fe의 표면에서 평가되었다. 그 결과 나노 Ta-Fe는 세포 부착, 증식에 우호적인 나노구조에 의해 향상된 세포친화성을 보였고, 세

포 독성과 조직 독성의 징후도 보이지 않음을 확인하였다. 이러한 결과는 장기적인 체내 안정성과 임상 효과를 지니는 Fe 기반의 정형 외과 임플란트의 실용화를 위한 가능성을 확인한 연구로, 동시에 TIPS 표면처리 기법의 가능성을 입증한 연구이다.

두 번째 연구에서는 항균 활성을 위해 코발트-크롬 합금 (Co-Cr) 임플란트 재료 표면에 TIPS를 통해 잠자리 날개의 나노 구조를 모방하였다. 금속 재료는 우수한 기계적 특성으로 인해 생물 의학 분야에서 유망한 재료이다. 이러한 장점에도 불구하고, 금속 임플란트의 낮은 항균성은 이의 사용을 제한하는 가장 큰 문제점으로 보고되어왔다. 낮은 항균특성을 가지는 임플란트 재료는 임플란트 주위염이나 골수염 등의 심각한 염증 반응이 유발하고 이로 인해 임플란트가 식립 위치로부터 탈락되어 재수술을 요하는 큰 문제점을 가진다. 이러한 문제점을 해결하기 위해 선행 연구에선 임플란트 재료 표면에 우수한 항균 특성을 보이는 은(silver)이나 항생제 등의 항균물질을 코팅 또는 함유시켜 금속 임플란트 표면에 우수한 항균 특성을 부여하는 연구가 적극적으로 이루어져왔다. 금속 임플란트 표면에 포함된 은, 항생제는 우수한 항균 효과를 나타내 염증을 억제하지만, 정상 세포에도 독성을 가지는 부작용으로 인해 그 사용이 제한되고 있다. 최근 잠자리 날개의 나노 구조가 박테리아의 세포 벽을 물리적으로 파괴하는 ‘기계적 항균 효과’를 보임이 입증되었다 (*Elena P. Ivanova et al.*). 본 연구는 기계적 항균 효과를 보이는 잠자리 날개의 나노구조를 TIPS 기술을 적용해 금속 임플란트

표면에 모방하여 은이나 항생제 사용 없이도 항균효과를 가지는 임플란트 재료 개발에 관한 연구이다. TIPS 기술을 적용해 잠자리 날개 모방 구조를 가지는 Nano-spike Co-Cr은 그람 음성균 및 그람 양성균 모두에 대하여 우수한 항균 효과를 나타냈을 뿐만 아니라, 강력한 골아 세포의 접착을 유도하는 나노 지형으로 인해 향상된 골아 세포 친화성도 동시에 보였다. 위에 명시한 본 연구의 접근법을 통해 우수한 항균효과와 생체적합성을 동시에 보이는 다기능성 임플란트를 개발하였다.

주요어(Keywords): 의료용 금속 임플란트, 탄탈륨, 생분해성 재료, 생체모방

학번: 2016-20810